8-1-2008

Quantification of carotid vessel wall and plaque thickness change using 3D ultrasound images

Bernard Chiu

Micaela Egger

J David Spence

Grace Parraga

Aaron Fenster

Quantification of carotid vessel wall and plaque thickness change using 3D ultrasound images

Bernard Chiu[a)]
Imaging Research Laboratories and Graduate Program in Biomedical Engineering, University of Western Ontario, London, Ontario N6A 5K8, Canada

Micaela Egger
Imaging Research Laboratories and Department of Medical Biophysics, University of Western Ontario, London, Ontario N6A 5K8, Canada

J. David Spence
Imaging Research Laboratories and Stroke Prevention and Atherosclerosis Research Centre of the Robarts Research Institute, University of Western Ontario, London, Ontario N6A 5K8, Canada

Grace Parraga and Aaron Fenster
Imaging Research Laboratories, Graduate Program in Biomedical Engineering, and Department of Medical Biophysics, University of Western Ontario, London, Ontario N6A 5K8, Canada

(Received 16 January 2008; revised 5 May 2008; accepted for publication 13 June 2008; published 17 July 2008)

Quantitative measurements of carotid plaque burden progression or regression are important in monitoring patients and in evaluation of new treatment options. 3D ultrasound (US) has been used to monitor the progression or regression of carotid artery plaques. This paper reports on the development and application of a method used to analyze changes in carotid plaque morphology from 3D US. The technique used is evaluated using manual segmentations of the arterial wall and lumen from 3D US images acquired in two imaging sessions. To reduce the effect of segmentation variability, segmentation was performed five times each for the wall and lumen. The mean wall and lumen surfaces, computed from this set of five segmentations, were matched on a point-by-point basis, and the distance between each pair of corresponding points served as an estimate of the combined thickness of the plaque, intima, and media (vessel-wall-plus-plaque thickness or VWT). The VWT maps associated with the first and the second US images were compared and the differences of VWT were obtained at each vertex. The 3D VWT and VWT-Change maps may provide important information for evaluating the location of plaque progression in relation to the localized disturbances of flow pattern, such as oscillatory shear, and regression in response to medical treatments. © *2008 American Association of Physicists in Medicine*.
[DOI: 10.1118/1.2955550]

I. INTRODUCTION

Stroke is the most common serious neurological problem in the world and the third leading cause of death among North American adults.[1] Direct and indirect costs of stroke are estimated to be $2.8 billion/year in the United States.[1] Clearly, stroke represents a staggering mortality, morbidity, and economic cost. Better ways to identify patients with increased risk for stroke, and better methods to treat and monitor them will have an enormous impact.

About 85% of strokes are ischemic, with most due to the blockage of a cerebral artery by a thrombotic embolus. Atherosclerosis at the carotid bifurcation is a major source of emboli, of either platelet aggregates (white thrombus) or atheromatous debris.[2,3] Most strokes associated with carotid atherosclerotic disease can be prevented by lifestyle/dietary changes, medical, and surgical treatment.[4,5] Improved identification of patients who are at risk for stroke, new strategies for treating atherosclerosis, and sensitive techniques for monitoring of carotid plaque response to therapy, will have a great impact on the management of these patients, and decrease the risk of stroke.

There is now agreement that for event-free survival, the important question is not simply related to the presence of disease or the degree of stenosis, but rather related to indolent slow progression and then sudden plaque complications leading to plaque rupture and consequent life- or brain-threatening thrombosis. Identification of factors responsible for the transformation of stable to ruptured plaques, and therapies that convert vulnerable to stable plaques has stimulated much research.[6–9]

The value of magnetic resonance imaging (MRI) in studies of carotid atherosclerosis is unquestioned.[10–12] MRI has been shown to be useful in measuring vessel wall area/volume,[13–15] assessing the state of the fibrous cap,[16–18] determining and classifying plaque composition,[19–21] and detecting plaque inflammation.[12,22,23] However, at present, MRI is costly and its scan time is long.[24–26] Thus, its use is primarily limited to symptomatic patients and for use in small-scale trials that require the use of imaging as the primary plaque monitoring modality in patients at risk for stroke, and who are being treated with plaque stabilization strategies. In addition, long scanning times increase the risk of image degradation due to subject motion.[27]

Doppler ultrasound (US) as a screening tool and its use in the assessment of stenosis severity is now unquestioned;[28] however, flow-velocity-based measurements of a single component at a few locations in the vessel provide indirect information on stenosis severity and no information on plaque morphology. Thus, it has a limited role in assessment of features of the arterial wall such as plaque vulnerability, changes, and composition.

The recent development of 3D US imaging techniques has allowed detailed examination of the 3D anatomical structure of the carotid artery,[29–32] and accurate measurements and quantification of carotid plaque. These measurements may aid in managing and monitoring patients,[33] and in evaluating the effect of new treatment options.[34] Different ultrasound phenotypes of carotid atherosclerosis have been assessed, such as carotid stenosis severity,[35] intima-media thickness (IMT),[36] plaque composition,[37] plaque area,[33] volume,[34,38–40] and plaque ulceration morphology and motion.[41,42] Although these metrics assist in the management of carotid atherosclerosis, they are single-valued measurements that do not provide sufficient information on the spatial distribution of plaques changes and burden in the carotid arteries. Information regarding the spatial distribution of carotid plaque changes could improve our understanding of plaque progression and regression in response to therapy.

The spatial distribution of arterial narrowing (stenosis) was studied by Barratt *et al.*[38] and Yao *et al.*[40] using 3D US imaging. Both researchers quantified the degree of stenosis by determining the ratio between the diameter (or area) of the lumen and the wall on each cross-sectional slice of the vessel. Yuan *et al.*[13] and Luo *et al.*[43] studied carotid plaque burden and luminal narrowing using high-resolution MRI by segmenting the vessel wall and lumen in MR images, which were acquired in serial cross sections. They presented their results using several parameters that summarized the vessel wall and lumen measurements for each patient: (1) maximum wall area, (2) location of the maximum wall area along the longitudinal axis of the carotid artery, (3) wall area in the common carotid artery (CCA) 3 mm proximal to the carotid bifurcation, (4) minimum lumen area, and (5) vessel wall volume. Although these five descriptive parameters are informative, they provided limited information regarding the spatial distribution of carotid plaque burden. The vessel wall and lumen measurements were obtained on a slice-by-slice basis in these investigations, but with the exception of the work by Barratt *et al.*,[38] these authors did not provide a slice-by-slice carotid plaque burden profile along the longitudinal direction of the vessel. The slice-by-slice stenosis profile provided by Barratt *et al.*[38] is useful in describing the distribution of plaque along the vessel; however, their stenosis profile only provided a single-valued description (percentage stenosis index) for each slice. Although this profile indicated the exact slices in which plaque burden was located, it gave no information as to where the plaque burden was located *within a slice*.

The major contribution of this paper is the introduction of a point-by-point *vessel-wall-plus-plaque thickness* (VWT) quantification technique, as well as a point-by-point VWT change quantification technique. A 3D map of the VWT-Change may provide important information to evaluate the location of plaque progression in relation to the geometry of the vessel and localized disturbances of flow pattern, such as oscillatory shear. Although the VWT is helpful in assessing the severity of the atherosclerotic lesion, the quantification of plaque burden progression or regression is more important in monitoring patients and in developing treatment strategies. Thus, in addition to evaluating the VWT at a single time point, we also developed a technique to compute the VWT-Change in the carotid artery between two imaging sessions. We report the VWT and VWT-Change measurements, obtained on a point-by-point basis, by mapping their respective values on the carotid vessel wall surface in order to show the localized nature of plaque thickness and plaque progression and regression.

Our quantification algorithm consists of several steps, which are shown in Fig. 1 as a schematic diagram. We applied our algorithm to the carotid artery phantom models[44] and the carotid arteries of six subjects to demonstrate the application of VWT and VWT-Change maps as new phenotypes to quantify progression/regression of carotid atherosclerosis.

II. METHODS

II.A. Segmentation method

Segmentation of the carotid artery can be done either manually or semiautomatically.[45] Since semiautomated carotid segmentation approaches using 3D US images have not yet been extensively validated, we tested our plaque quantification algorithm using the manual segmentations performed by a trained observer (ME). It has been well established that the double-line pattern corresponds to the lumen-intima (i.e., the lumen boundary) and media-adventitia interfaces (i.e., the wall boundary) in the longitudinal view of *B*-mode ultrasound images, which is the view typically used for the measurement of IMT.[46] Comparisons of ultrasound to histological measurements of the intima plus media layers have been shown to correspond.[47–50] In the longitudinal view of *B*-mode ultrasound images, the lumen is echolucent with the adjacent echogenic boundary representing the lumen-intima boundary, and the second echogenic boundary representing the media-adventitia boundary. Using 3D US, it is possible to view images as shown in Fig. 2(a) in both the longitudinal and transverse view in order to identify the correspondence between the longitudinal media-adventitia boundary, as well as in the transverse view [Fig. 2(b)].

Although the manual segmentation method used in obtaining the wall and lumen measurements may make a larger clinical trial laborious, until a semiautomated technique is validated and generally accepted, manual techniques must still be used, and, in fact, are being used in our clinical trials.[34,51] In any case, validation of new segmentation algorithm will require manual segmentation results. However, it is important to point out that our proposed quantification method is equally applicable to boundaries segmented by

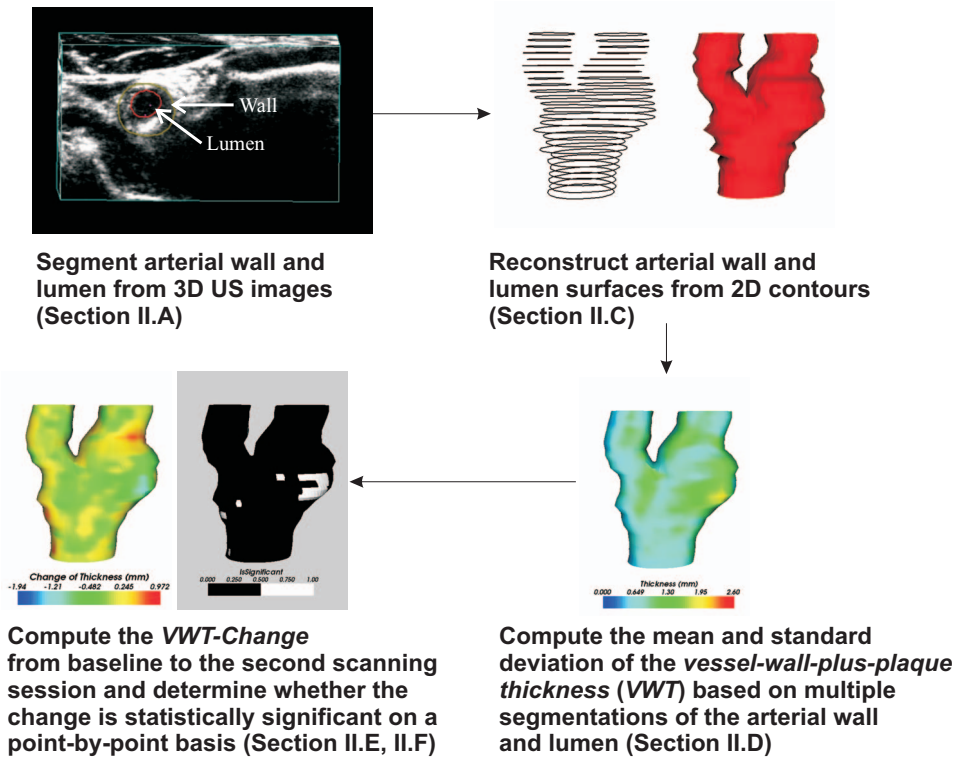

FIG. 1. Schematic diagram showing the steps of the proposed algorithm in generating 3D *vessel-wall-plus-plaque thickness* (VWT) map (with the section numbers in which they are explained).

semiautomatic or fully automatic segmentation algorithms, and the purpose of applying our algorithm on manually segmented boundaries is mainly to demonstrate the application of the proposed quantification algorithm.

Since the expert observer segmented the carotid arteries on a slice-by-slice basis, the segmentation results may exhibit an accordion-like shape (i.e., adjacent contours shrink and expand) because of segmentation variability [see Figs. 3(b) and 3(e)]. In order to avoid this problem, the trained observer segmented the vessel wall and lumen in each 3D US image five times to provide information on the segmentation variability and allow statistical testing of any observed change in VWT. In each segmentation session, the carotid bifurcation was located, and an axis was placed parallel to the longitudinal axis of the common carotid artery. The 3D US images were resliced at 1 mm intervals by transverse planes that were perpendicular to the longitudinal axis, and segmentation was performed on each 2D transverse image [Fig. 2(b)].[52] Since the orientation of the longitudinal axis selected in each segmentation session is slightly different, repeated vessel wall and lumen segmentations for a single 3D US image were performed in slightly different transverse planes [e.g., two of the five repeated vessel wall segmentations were drawn in white and black outlines in Fig. 4(a)]. For this reason, we needed to reconstruct the 3D surface meshes from 2D contours produced in the five segmentation sessions, and reslice the five surface meshes using the same

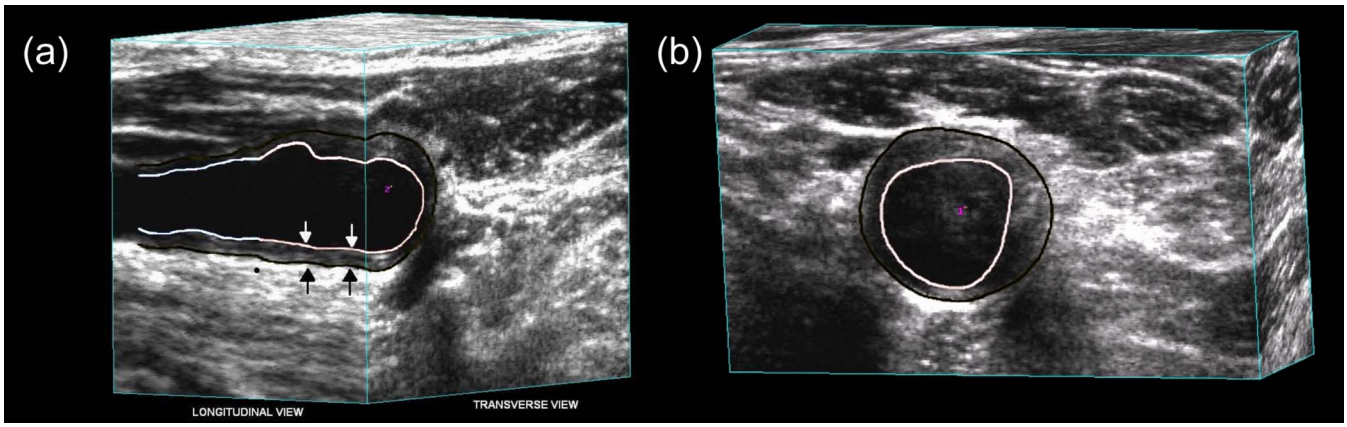

FIG. 2. (a) 3D US image of carotid artery showing both the longitudinal and transverse views. The black arrows correspond to the media-adventitia boundary and the white arrows correspond to the lumen-intima boundary. (b) 3D US transverse view with the media-adventitia and lumen-intima boundaries manually outlined.

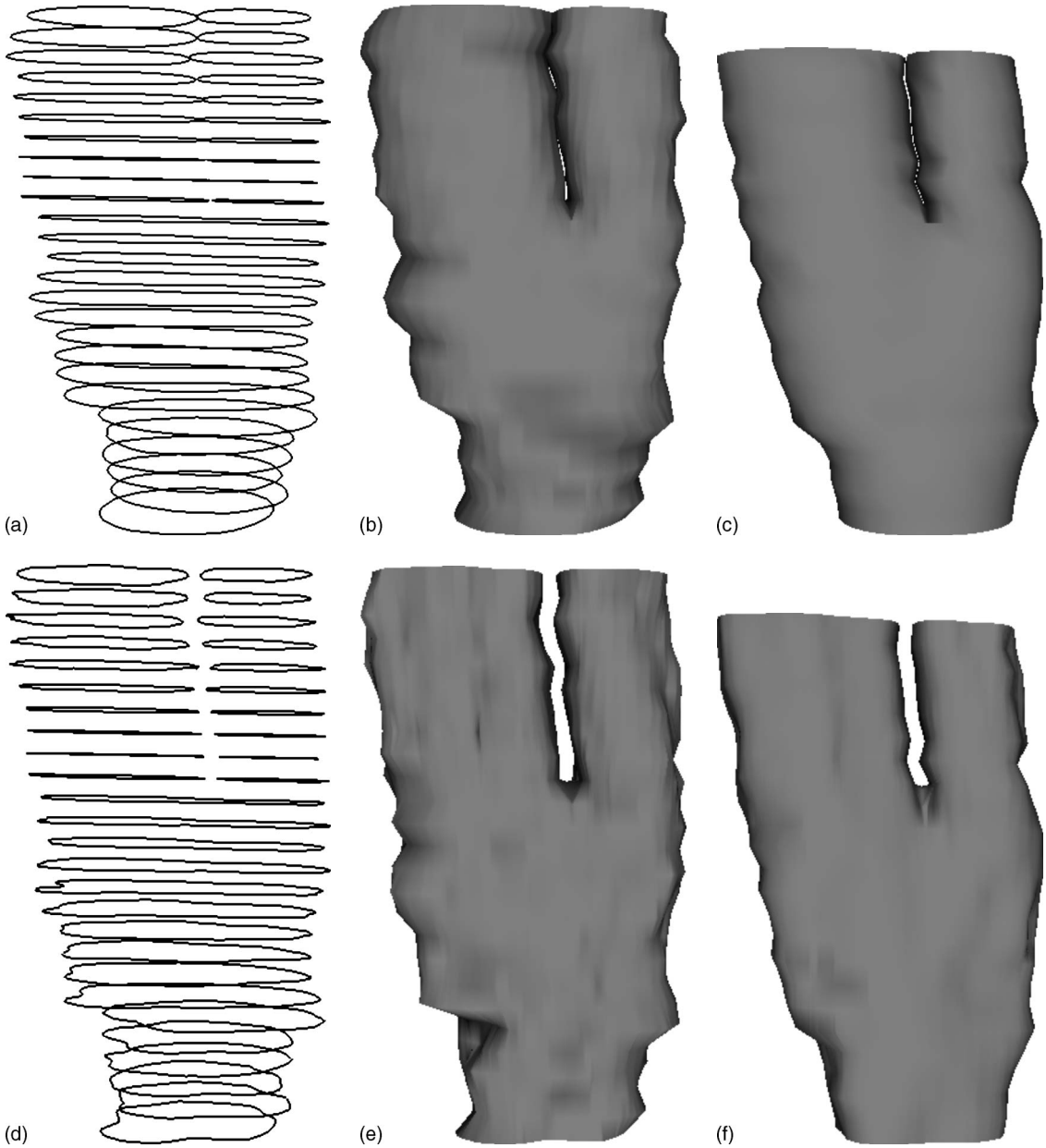

FIG. 3. A demonstration of the proposed surface reconstruction method and the mean surface computation algorithm. (a) Segmentation of the arterial wall produced in one segmentation session, (b) the corresponding reconstructed surface, and (c) the mean surface of the arterial wall, computed from segmentation results produced in five sessions. (d) Segmentation of the arterial lumen produced in one segmentation session, (e) the corresponding triangulated surface, and (f) the mean surface of the arterial lumen.

2D plane to produce five 2D contours before we were able to compute the mean and the standard deviation of the VWT [see Sec. II D].

II.B. Surface matching using symmetric correspondence

The matching of the arterial wall (media-adventitia interface) and the lumen (blood-intima interface) boundaries obtained at each of the time points is required before the VWT map could be constructed. In this work, we matched the wall and the lumen surfaces using a modified version of the symmetric correspondence algorithm developed by Papademetris *et al.*[53] The distance between each pair of correspondence points matched by the algorithm represents a local estimate of the VWT (i.e., the combined thickness of the plaque, intima, and media).

Many surface (or curve in 2D) correspondence definitions have been proposed. Cohen *et al.*[54] minimized an objective function that integrated the difference between the curvatures of all corresponding pairs. Tagare[55] pointed out that the objective function defined by Cohen *et al.*[54] depended on the choice of the domain of integration, which was arbitrarily chosen (i.e., a correspondence map that minimizes the objective function computed over the domain of the first curve is not equal to that of the second curve). This asymmetric correspondence problem was addressed in Papademetris *et al.*[53]

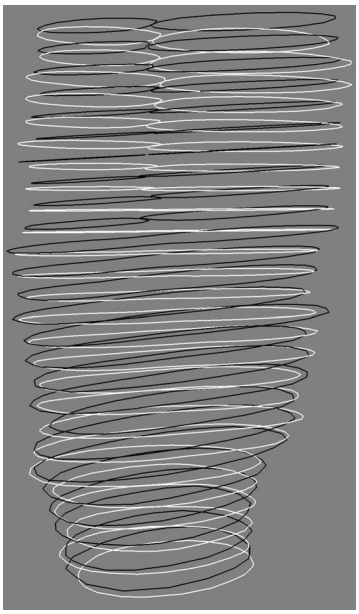

FIG. 4. Demonstration that surface reconstruction is required before computing the mean surface. Two of the five repeated vessel wall segmentations were drawn in white and black outlines. Because repeated vessel wall segmentations for a single 3D ultrasound image are performed in slightly different transverse planes, the 3D surfaces from contours produced in five segmentation sessions first need to be reconstructed, and then the five surface meshes resliced using a common 2D plane, before the mean surface can be computed.

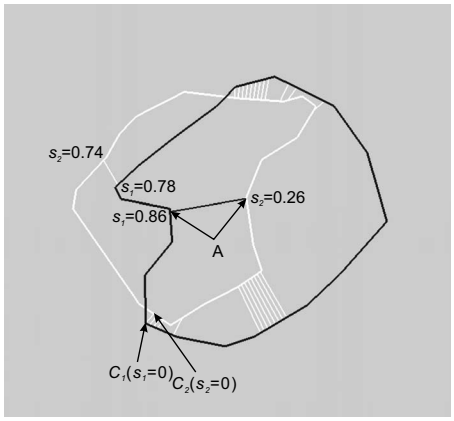

(a)

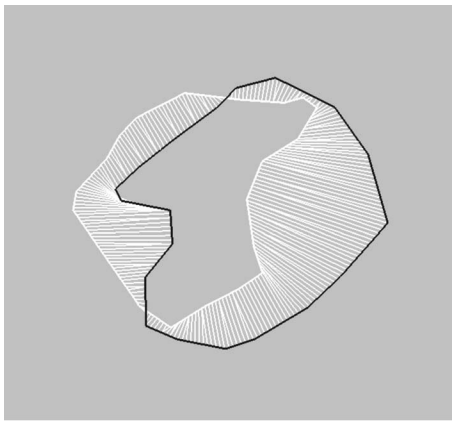

(b)

FIG. 5. A demonstration of the proposed modification to the symmetric correspondence algorithm of Papademetris *et al.* (Ref. 53). The two curves to be matched are drawn in black and white, respectively, in (a). The line segments connect the symmetric corresponding pairs obtained using the algorithm proposed by Papademetris *et al.* (Ref. 53). The arclength parameters s_1 and s_2 of the curves C_1 and C_2 start from $C_1(0)$ and $C_2(0)$, respectively, and increases in the counterclockwise direction. A comparison of the corresponding pair indicated by A ($s_1=0.86$, $s_2=0.26$) and the previous corresponding pair, with $s_1=0.78$ and $s_2=0.74$, shows that the pair A (represented by a black line) is associated with a much smaller s_2. To guarantee one-to-one mapping, the function ϕ that maps s_1 to s_2 must be an increasing function. Thus, the pair A is discarded in our algorithm. Vertices without symmetric nearest neighbors were paired by interpolation (Ref. 53), resulting in the corresponding pairs joined by white lines in (b).

and the authors proposed a symmetric correspondence algorithm. Although corresponding pairs found using Papademetris's algorithm are symmetric, one-to-one correspondence mapping between two curves is not guaranteed. In our paper, we propose a modification to Papademetris's algorithm so that the symmetric correspondence mapping is always one-to-one.

A correspondence map between two curves can be described using a mapping, ϕ, that maps s_1 to s_2, where s_1 is the arclength parameter of curve C_1, and s_2 is that of a second curve C_2. A one-to-one correspondence map must be either a monotonically increasing or decreasing function depending on the orientation of the arclength parametrization, as long as two curves are of the same topology (i.e., closed curves here). Without loss of generality, suppose that two curves are of the same orientation with respect to their arclength parametrization (one can always reparametrize one curve to make the orientation the same), then ϕ must be a monotonically increasing function. This condition is not guaranteed to be satisfied for the corresponding pairs determined using Papademetris's algorithm[53] as shown in Fig. 5. The line segments in Fig. 5(a) connect the symmetric corresponding pairs. The corresponding pair indicated by A [$s_1=0.86$, $s_2=\phi(s_1)=0.26$] is associated with a much smaller s_2 compared to that of the previous corresponding pair with arclength parameters $s_1=0.78$ and $s_2=\phi(s_1)=0.74$, indicating that ϕ is decreasing. To make sure the correspondence mapping is one-to-one, this is not allowed in our proposed modification, and the corresponding pair A is discarded. After obtaining all the allowable symmetric corresponding pairs, we paired the vertices without symmetric nearest neighbors by arclength interpolation,[53] resulting in the corresponding pairs joined by white lines shown in Fig. 5(b).

II.C. Reconstructing surfaces from manually segmented contours

To reconstruct the surface for the internal, external, and common carotid arteries (ICA, ECA, and CCA, respectively), the symmetric correspondence algorithm described in Sec. II B was used to pair the vertices on adjacent 2D contours. Since the number of vertices on a segmented contour was determined by the expert observer according to the shape of the boundary (i.e., more points were used to segment more complex shapes and fewer points to segment simpler ones), the number of vertices for adjacent segmented

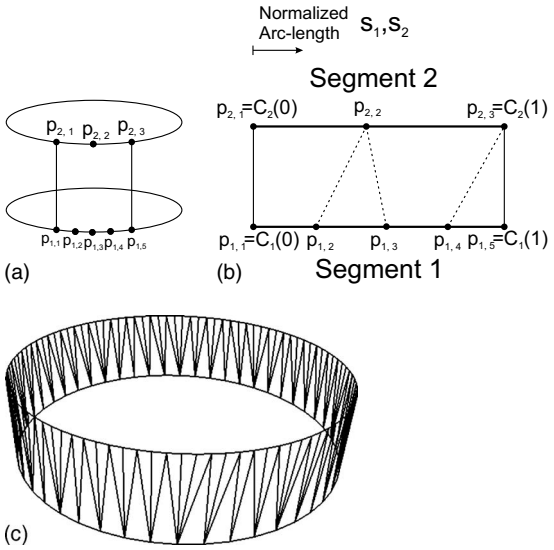

FIG. 6. Schematic diagrams showing how unpaired vertices are connected in reconstructing a surface from segmented contours. (a) The segments on two contours that are between two corresponding pairs (i.e., $p_{1,1}\leftrightarrow p_{2,1}$ and $p_{1,5}\leftrightarrow p_{2,3}$). There are three vertices on Segment 1 and one vertex on Segment 2 that have no corresponding points. (b) The ith vertex of Segment 1, $p_{1,i}$, is assigned to be the corresponding point of the jth vertex of Segment 2, $p_{2,j}$, if the absolute difference of the normalized arclength between them is the minimum among all points $p_{2,k}$ on Segment 2. (c) The surface that was reconstructed from two circles of unity radius with different number of vertices. The bottom circle consists of 50 vertices and the top circle consists of 100 vertices.

contour would likely be different. Therefore, our surface reconstruction algorithm must allow the flexibility of connecting contours with different number of points. For this reason, we used the following scheme to pair vertices without a symmetric corresponding point, instead of using the arclength interpolation technique described in Sec. II B. This scheme ensures that no vertex selected by the expert observer during segmentation would be discarded as a result of the surface reconstruction procedure. This scheme of connecting unpaired vertices only applied to reconstructing surfaces, while in other sections in which the symmetric corresponding algorithm was used, the arclength interpolation scheme was applied.

II.C.1. Connecting vertices without symmetric corresponding points

Figure 6(a) shows segments on two contours that are between two corresponding pairs (i.e., $p_{1,1}\leftrightarrow p_{2,1}$ and $p_{1,5}\leftrightarrow p_{2,3}$). There are three vertices on one contour segment and one vertex on the other segment that have no corresponding points. The segment that has more vertices that are without correspondence was chosen, and denoted as Segment 1. The other segment was denoted as Segment 2. The length of Segments 1 and 2 are first normalized to 1 [Fig. 6(b)]. We define two mappings C_1 and C_2 that map Segments 1 and 2 from their normalized arclength to their 3D coordinates, i.e., $C_1: s_1 \rightarrow p_1$ and $C_2: s_2 \rightarrow p_2$, where $s_1, s_2 \in [0,1]$ and $p_1, p_2 \in R^3$. The ith vertex of Segment 1, $p_{1,i}$, is assigned to be the corresponding point of the jth vertex of Segment 2, $p_{2,j}$, if the absolute difference of the normalized arclength between them is the minimum among all points $p_{2,k}$ on Segment 2, i.e.,

$$|C_1^{-1}(p_{1,i}) - C_2^{-1}(p_{2,j})| = \min_{k\in\{1,\ldots,N_2\}} |C_1^{-1}(p_{1,i}) - C_2^{-1}(p_{2,k})|, \quad (1)$$

where C_1^{-1} and C_2^{-1} are the inverse mapping of C_1 and C_2, respectively, and N_2 is the total number of points on Segment 2 [e.g., $N_2=3$ in Fig. 6(b)].

After all corresponding points have been established, the quadrilaterals between two corresponding pairs [e.g., $p_{1,1}$-$p_{2,1}$-$p_{2,2}$-$p_{1,2}$ and $p_{1,3}$-$p_{2,2}$-$p_{2,3}$-$p_{1,4}$ in Fig. 6(b)] were triangulated to form a triangular mesh. Figure 6(c) shows an example of a surface mesh that was reconstructed from two circles of unity radius. The bottom circle consists of 50 vertices and the top circle consists of 100 vertices.

II.C.2. Surface reconstruction at the carotid bifurcation

Near the bifurcation apex of the carotid artery, the ICA and ECA merge to the CCA, and since the symmetric correspondence algorithm was designed to pair corresponding points of one closed curve to another, it could not be used unless the CCA slice immediately proximal to the apex was divided into two closed curves. This was achieved by using the method depicted in Fig. 7. First, the centroids of the ICA and ECA slices immediately distal to the apex (C_{ICA} and C_{ECA}) were computed and joined together by a line, which intersects the ICA and ECA slices at I_i and I_e, respectively [see Figs. 7(a) and 7(c)]. The position of the bifurcation apex must be between the plane cutting the CCA slice and that cutting the ICA and ECA slice. In the proposed algorithm, it was chosen to be 0.1 mm below the midpoint of I_e and I_i [see Figs. 7(c) and 7(d)]. We computed the tangents of both the ICA slice at I_i and the ECA slice at I_e and, consequently, the average directions of the two tangents. A line pointing to the average direction and passing through the midpoint between I_i and I_e was defined and projected onto the plane containing the CCA slice. This projected line intersects the CCA slice at two points, which, together with the bifurcation apex, were interpolated by a Cardinal spline to produce an arch. The number of vertices representing this arch was determined in a way such that the interval between vertices is approximately the same as that of the CCA slice. The CCA slice was then divided into two closed curves, C_1 and C_2 as shown in Figs. 7(b) and 7(d), by this arch. Then, C_1 was paired with ECA, and C_2 with ICA, using our method described in Secs. II B and II C 1.

Figure 3(b) shows the tessellated surface constructed from the stack of 2D contours of the arterial wall shown in Fig. 3(a). Figure 3(e) shows the surface constructed for the contour set representing the carotid lumen shown in Fig. 3(d).

II.D. Mean and standard deviation of VWT

After segmenting the vessel wall and lumen five times in each slice of the 3D image, we reconstructed the boundaries

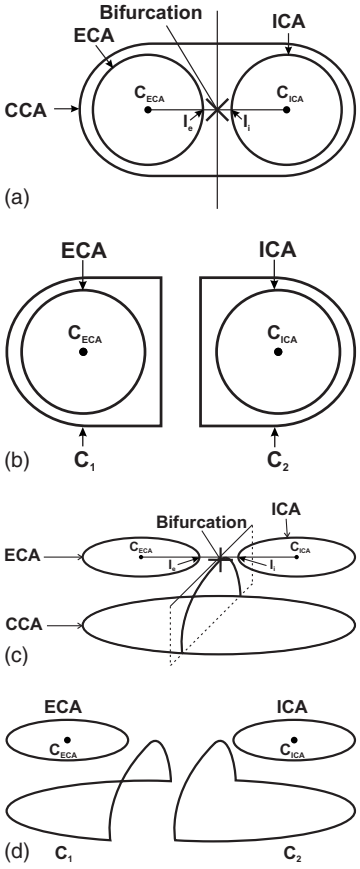

FIG. 7. Reconstruction of the arterial vessel surface at the bifurcation apex. (a) and (c) Two different views at the same carotid artery bifurcation. In our algorithm, the CCA slice immediately proximal to the bifurcation apex is split into two closed curves [shown as C_1 and C_2 in (b) and (d)], so that the correspondence mapping can be established between the ECA slice and C_1, and between the ICA slice and C_2. C_{ECA} and C_{ICA} are the centroids of the ECA and ICA slices and the line joining these two points intersect the ECA slice at I_e and the ICA slice at I_i [see (a) and (c)].

obtained at each session to form a surface according to Sec. II C, resulting in five surfaces representing the wall and five representing the lumen. The following steps were used to calculate the mean and standard deviation of VWT:

(1) As mentioned in Sec. II A, the longitudinal axis of the vessel was chosen in each of the five segmentation sessions, and this axis defined the normal of the transverse cutting plane used for reslicing in each segmentation session. In defining the surface mean and standard deviation, we first defined a common transverse cutting plane used to reslice the five surfaces. The normal of this common transverse plane was computed by averaging the normals of the five manually identified longitudinal axes. The five segmented arterial wall and the five arterial lumen surfaces were resliced at 1 mm intervals using this common transverse plane, and it resulted in five 2D contours for the wall segmentations and five for the lumen [Fig. 8(a)].

(2) The mean contours for the wall and lumen boundaries were calculated separately, but in the same manner described in the following: One of the five curves, denoted by C_1, obtained in Step 1 was chosen. The symmetric correspondence mappings were established between C_1 and the remaining four curves. The choice of C_1 is quite arbitrary and this choice should not have a significant impact on the shape of the mean boundary and its standard deviation. However, a consistent choice should be defined in our algorithm. In making this choice, we observed that the boundaries of carotid vessel are smooth and approximately circular. Thus, we determine C_1 based on the circularity ratio (CR), computed by the equation $4\pi A/P^2$, where A is the area enclosed by the curve (in square millimeters) and P is the perimeter of the curve (millimeters). A circle has the maximum CR, equalling to 1. Thus, we chose C_1 as the boundary that has the highest CR. After the symmetric correspondence algorithm has been applied, each point on C_1 is associated with its corresponding points on the remaining four curves. These groups of five corresponding points are denoted by $\{p_i : i=1,2,\ldots,5\}$ [Fig. 8(a)]. The averages of these five-point groups were connected to form the mean curve [see the red curve in Fig. 8(a)].

(3) After the mean curves for the wall and lumen had been obtained, the symmetric correspondence mapping was established between these two mean curves.

(4) The mean VWT at a point on the arterial wall was defined to be the distance from this point to its corresponding point on the arterial lumen [see Fig. 8(b) and an example in Figs. 13(b) and 13(d)—discussed in Sec. IV]. Each pair of corresponding points, denoted by p_w and p_l in Fig. 8(b), defined a line, which was used to intersect the five contours of the wall and lumen. The distances between each of the five intersections on the wall segmentations and p_w, and those between each of the five intersections on the lumen segmentations and p_l were obtained. The standard deviation of the first set of five distances was calculated and used to quantify the standard deviation of the wall segmentations, and that of the second set of five distances gave the standard deviation of the lumen segmentations.

Then, we reconstructed the mean wall and mean lumen surfaces from the mean contours obtained using the surface reconstruction method described in Sec. II C. Figures 3(c) and 3(f) show an example of the mean arterial wall and lumen surfaces, which are averaged from five segmentations from a *single* 3D US image, and are much smoother than the respective surfaces obtained in one segmentation session [Figs. 3(b) and 3(e)]. Figure 8(b) shows an example of the five segmentations for the wall (in black) and five for the lumen (in grey). The mean boundaries of the wall and lumen were represented by the red curves. The inset of Fig. 8(b) shows the intersections between the line connecting a corresponding pair, and the five wall and five lumen segmentations.

II.E. Computation of the VWT-Change map

In monitoring change in the carotid arteries, a patient's carotid vessel must be imaged at two 3D US scanning

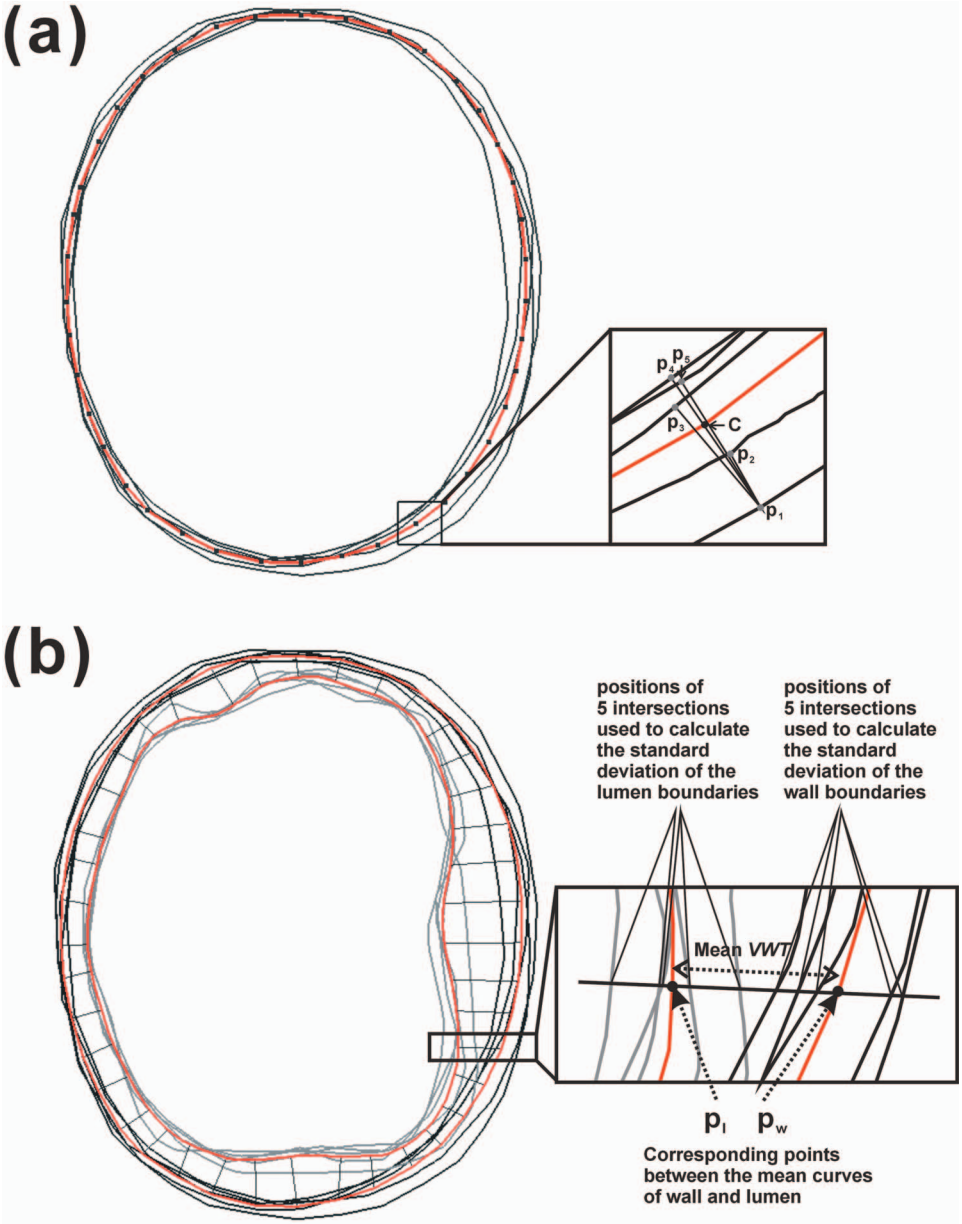

FIG. 8. Method of computation for the mean and standard deviation of the vessel-wall-plus-plaque thickness (VWT). (a) How a mean contour was calculated from five segmented contours of the arterial wall (black curves). The red curve is the mean wall contour. The average of five corresponding points $\{p_i : i = 1, 2, \ldots, 5\}$ on five segmented contours was computed, and all average points thus computed define the mean contour. (b) The black curves are the five segmentations of the arterial wall, and the grey curves are the five segmentations of he arterial lumen. The outer and inner red curves represent the mean arterial wall and lumen, respectively. A pair of corresponding points between these two curves defines a line. This line intersects the wall and lumen boundaries, and these intersections are used to calculate the standard deviation of the positions of the wall and lumen boundaries. The standard deviation of VWT was then computed based on these two standard deviations.

sessions.[34] Analysis of changes in the vessel requires that the average carotid artery surfaces be appropriately registered. A modified version of the iterative closest point (ICP) algorithm by Besl *et al.*[56] was used for this purpose. Instead of aligning the centroids of the two surfaces as proposed in Besl *et al.*,[56] we aligned the bifurcation apex of the carotid vessels, which was determined in Sec. II C (Fig. 7). We then used the ICP algorithm[56] to find the optimal rotation by iteratively matching points on the two surfaces to be registered and finding the least-square rigid body transformation. The iteration continued until the root-mean-square of the distances between the matched points on the two surfaces was below a preset threshold, which was set at 10^{-4} mm.

In Sec. II D, the VWT at each point of the carotid wall surface was computed. To obtain the VWT-Change map, points on the two carotid wall surfaces must be matched. We established correspondence between two points with the same angular position, θ, with respect to the centroid of the 2D slice. The ray-casting method[57] could be used to determine the angular position, θ, of each point in the 2D slice, in which a ray is cast from the centroid of the curve at the angle θ to intersect the 2D slice; however, the ray-casting method

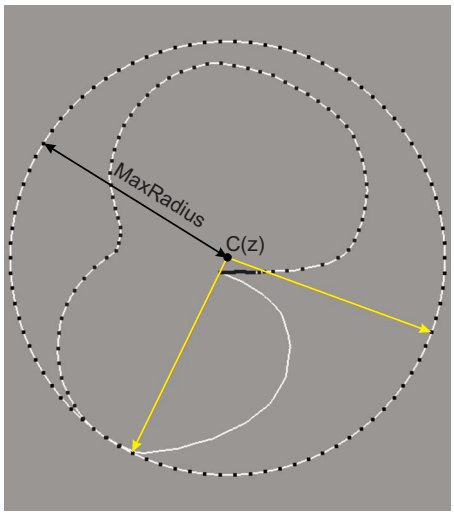

(a)

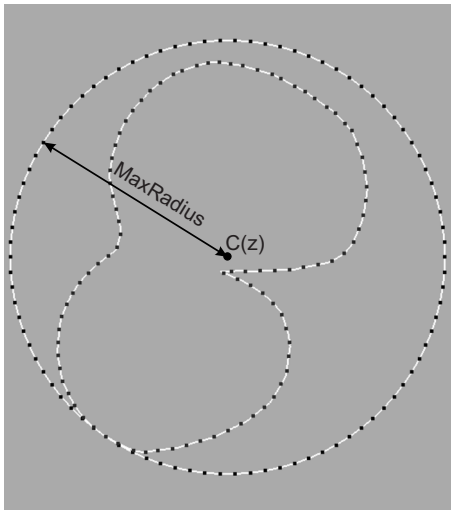

(b)

FIG. 9. The purpose of resampling the mean wall contours angularly is to establish corresponding points between the two VWT maps, needed when computing the VWT-Change map. The circle with MaxRadius, the maximum distance from the centroid, $\mathbf{C}(\mathbf{z})$, to the contour boundary, and the contour to be resampled are drawn in (a) and (b). The black dots on the contour represent the angularly resampled points. (a) The points resampled by applying the ray-casting method, in which a ray is cast from the centroid in a uniform angular interval. Note that about 25 sampled points are clustered between the two rays drawn. (b) The angular positions of points on the same contour computed by the proposed method. The proposed angular resampling method produces points that are evenly distributed along the curve.

cannot space points uniformly on complex contours, as found when examining the carotid arterial wall near the bifurcation apex [see Fig. 9(a)]. Thus, we defined the angular position of each point on the boundary using the following procedure [Fig. 9(b)]:

(1) Find the centroid of the 2D slice of the artery wall surface, $\mathbf{C}(\mathbf{z})$, where $\mathbf{z}$ represents the axial distance from the bifurcation apex (positive value of $\mathbf{z}$ represents location distal and negative value of $\mathbf{z}$ represents location proximal to the bifurcation).
(2) Find the maximum distance between $\mathbf{C}(\mathbf{z})$ and the boundary of the 2D slice and label it MaxRadius.
(3) Define a circle centered at $\mathbf{C}(\mathbf{z})$ and with MaxRadius as the radius. The circle is represented by points with constant angular interval between them. The angular position, θ, of each point, $\mathbf{x}$, on the circle is defined by the angle between the line from C_{ECA} to C_{ICA} and that from $\mathbf{x}$ to $\mathbf{C}(\mathbf{z})$ (see Fig. 9).
(4) Use the symmetric correspondence algorithm to match the circle defined in Step (3) and the 2D slice. The angular position, θ, of each point in the 2D cross section of the arterial wall is assigned to be that of its corresponding point on the circle.

The angular positions were computed for the carotid artery mean wall associated with the 3D US images acquired in the two scanning sessions. The points on the same 2D transverse slice of the two carotid vessel surfaces associated with the first and second 3D US images were matched according to the angular positions. For each pair of corresponding points, the VWT-Change was computed, color-coded, and superimposed on the arterial wall [see the examples in Figs. 14(c) and 14(g) and Figs. 15(c) and 15(g)—discussed in Sec. IV].

II.F. t-test on VWT changes

We determined the statistical significance of the difference by the two-sample Student's t-test. Since we are performing multiple hypothesis tests, each for a single vertex on the VWT map, we need to compute α, the per-comparison error rate (i.e., probability of Type I error in a single test), that is required to keep the family-wise error rate (i.e., the probability of committing one or more Type I errors) to be less than $\hat{\alpha}$:[58]

$$\alpha = 1 - (1 - \hat{\alpha})^{1/N}, \tag{2}$$

where N is the total number of independent tests performed, which is equal the total number of points on the VWT map. Note that Bonferroni correction $(\alpha = \hat{\alpha}/N)$[59] is commonly used to approximate α. It takes into account only the first two terms in the MacLaurin Series of the term $(1-\hat{\alpha})^{1/N}$ in Eq. (2).

The two-sample t-test involves testing the equality of means of two random variables, which, in our case is the mean VWT at time points 1 and 2, denoted by $\{\overline{T_i}: i=1,2\}$ and expressed in terms of the mean wall positions, $\{\overline{W_i}: i=1,2\}$, and the mean lumen boundary positions, $\{\overline{L_i}: i=1,2\}$:

$$\overline{T_i} = \overline{W_i} - \overline{L_i}, \quad i = 1,2, \tag{3}$$

where $\overline{W_i}$ and $\overline{L_i}$ are assumed to be normally distributed with standard errors $s_{W,i}/\sqrt{n}$ and $s_{L,i}/\sqrt{n}$, respectively, where $s_{W,i}$ and $s_{L,i}$ are the standard deviation of the positions of the wall boundaries and that of the lumen boundaries, computed at

time point i (=1 or 2), and n is the number of boundaries, equals to 5 in our experiments.

The standard error, s.e., and the degrees of freedom. ν, are needed for the t-test. Since the VWT-Change, D, equals $\overline{T_2}$ subtracted by $\overline{T_1}$, D has a t distribution with s.e. and ν expressed by Eqs. (4) and (5). The reader is referred to Satterthwaite[60] for the computation of the degrees of freedom.

$$\text{s.e.} = \sqrt{\frac{s_{W,1}^2 + s_{L,1}^2 + s_{W,2}^2 + s_{L,2}^2}{n}}, \tag{4}$$

$$\nu = \left(\frac{s_{W,1}^2 + s_{L,1}^2 + s_{W,2}^2 + s_{L,2}^2}{n} \right)^2 \Bigg/ \frac{(s_{W,1}^2/n)^2 + (s_{L,1}^2/n)^2 + (s_{W,2}^2/n)^2 + (s_{L,2}^2/n)^2}{n-1}. \tag{5}$$

III. EXPERIMENTAL METHODS

III.A. Test phantom experiments

Two anthropomorphic test phantoms of the human carotid arteries were used to validate the accuracy of the VWT map computed by our algorithm. Since the VWT is defined to be the distance between a corresponding pair of vertices consisting of a vertex on the vessel wall and a second vertex on the arterial lumen, this experiment also serves as a test of the surface correspondence algorithm described in Sec. II A. We used a carotid arterial model, which was obtained by averaging the radii of the lumen boundaries outlined from x-ray angiograms of 62 patients with different stenosis grades (determined by the NASCET stenosis index), to validate the VWT measurements.[44] Since the purpose of this phantom study was only to validate the accuracy of the VWT measurements, and not the US imaging techniques, no US scanning or segmentation was performed. In this experiment, we used the normal and 30%-stenotic arterial models as the arterial lumens, which were provided to us by the authors of Ref. 44 as a CAD model. The arterial wall model [blue surface in Fig. 10(a)] was constructed by expanding the normal arterial phantom [red surface in Fig. 10(a)] on a slice-by-slice basis, and then reconstructed using the surface reconstruction technique described in Sec. II C. Then, the VWT measurements were obtained and validated for these two models.

III.B. Evaluation using patient 3D US images

III.B.1. 3D US image acquisition

The 3D US images were acquired using a motorized linear mover to translate the US transducer (L12-5, 50 mm, Philips, Bothel, Washington) continuously along the neck of the subjects without cardiac triggering. The stiffness of the carotid artery (a dimensionless quantity defined by Kawasaki *et al.*[61]) increases with age and with progression of atherosclerosis. A study involving healthy nonsmoking Caucasian female volunteers[62] reported that the stiffness of the CCA increases from 3.5 in the subject group of mean age 15 years to 11.3 in the subject group of mean age 79 years, and the arterial strain, which is a dimensionless quantity also known as the fractional diameter change, decreases from 0.11 in the younger group to 0.05 in the older group. Changes in plaque morphology during the cardiac cycle are also a consideration. Van Popele *et al.*[63] reported that the distensibility coefficient of the common carotid artery is lower in subjects who have severe plaque lesions. Since our study dealt with older subjects (69 ± 6 years for one population and 70 ± 10 years for the other) with atherosclerosis, we decided against using cardiac gating, which may lead to the lengthening of the scan time, increasing the susceptibility to involuntary patient head motion and swallowing.

The US probe was moved along the neck at a uniform speed for an approximate length of 4.0 cm, which requires approximately 8 s. Since the US probe was held by a mechanical assembly, the transducer angle was fixed to be per-

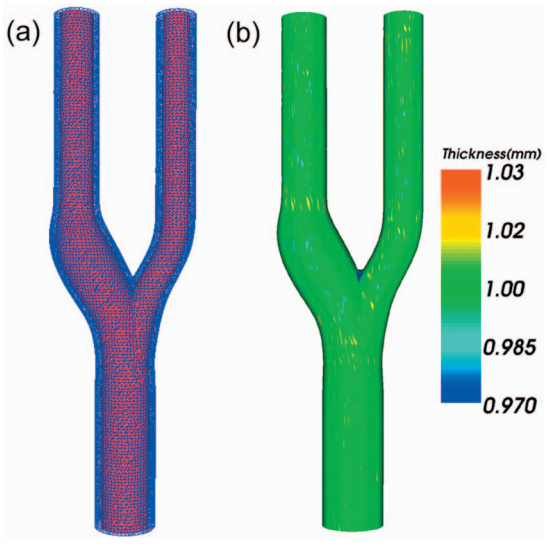

FIG. 10. The VWT map was validated using test phantoms models. (a) The blue surface mesh represents the arterial wall and the red surface represents the arterial lumen. The normal carotid artery phantom model in Smith *et al.* (Ref. 44) was used as the arterial lumen (red), which was expanded by 1 mm to produce the arterial wall (blue). (b) The VWT map showing the thickness between the arterial wall and lumen shown in (a).

pendicular to the skin and the direction of the scan for all patient scans. The video frames from the US machine (ATL HDI 5000, Philips, Bothel, Washington) were digitized and reconstructed into a 3D image, which was displayed using the 3D viewing software developed in our laboratory.[64,65] The resulting 3D image has a pixel size of 0.1 mm $\times$0.1 mm$\times$0.15 mm. It is important to note that since the 3D US image has been reconstructed as a volume that allows us to reslice at any oblique angle, the US acquisition plane did not constrain our choice of the reslicing plane used for carotid segmentation.

III.B.2. Study subjects

We demonstrated the use of our approach using 3D US carotid images of two groups of subjects with three in each group. The 3D carotid US images of the subjects in Group 1 were acquired at base line and 3 months later. These subjects (who participated in a clinical study focusing on the effect of atorvastatin[34]) were asymptomatic with carotid stenosis $>$60% (according to the carotid Doppler flow velocities),[34] and received 80 mg of atorvastatin daily during the interval between the two scanning sessions. The statin therapy was shown to reduce the size of the atherosclerotic plaque.[34] In the study by Ainsworth *et al.*,[34] 17 subjects had been treated by atorvastatin, from which we chose three subjects for this study to reflect a wide spectrum of plaque volume changes: Subject 1 had the largest, Subject 2 had a moderate, and Subject 3 had the smallest plaque volume change.

The 3D carotid US images of the subjects in Group 2 (Subjects 4, 5, and 6) were acquired at base line and 2 weeks later. These subjects were recruited from The Premature Atherosclerosis Clinic and The Stroke Prevention Clinic at University Hospital (London Health Sciences Centre, London, Canada) and the Stroke Prevention and Atherosclerosis Research Centre, Robarts Research Institute for an interscan vessel-wall-volume reproducibility study performed by Egger *et al.*[52] These subjects received no treatment at the interval between the two scanning sessions, and no change in the plaque burden was expected. Egger *et al.*[52] have shown that interscan reproducibility of the vessel-wall-plus-plaque volume (VWV) measurements was high. We have segmented the wall and the lumen five times each for all 12 3D US scans (i.e., 6 patients$\times$2 scan/patient—one scan for time point 1, the other for time point 2). Then we evaluate the reproducibility of the VWT measurements for this group of subjects by analyzing the VWT-Change map (Sec. II E) and the t-test results (Sec. II F).

All subjects gave consent to the study protocol approved by The University of Western Ontario standing board of human research ethics. By comparing the results obtained from these two groups of patients, we aim to demonstrate that the spatial distribution of the VWT-Change can be calculated and displayed, and that the statistical significance of the VWT-Change can be evaluated.

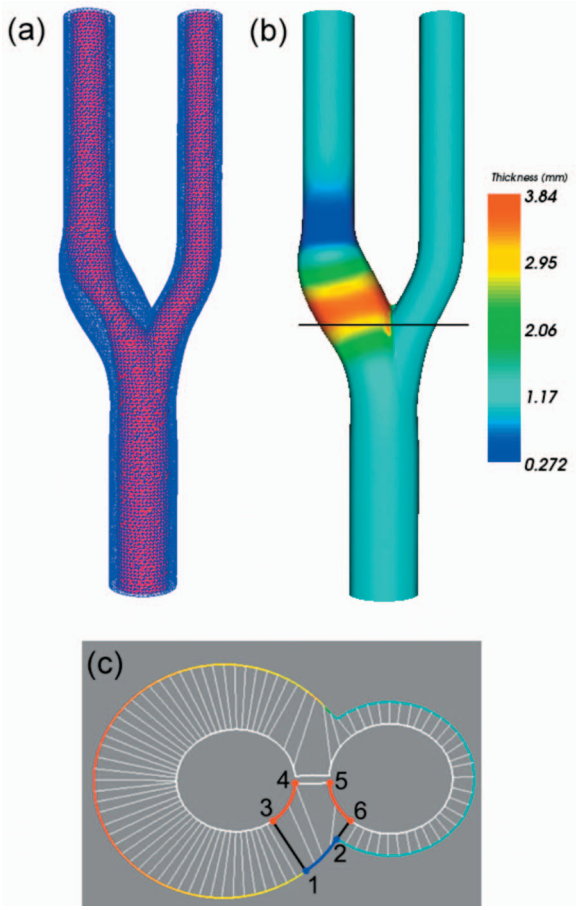

FIG. 11. (a) The expanded normal artery was used as the arterial wall and the 30%-stenotic artery was used as the arterial lumen. (b) The VWT map computed for the wall and lumen shown in (a) has been color-coded and mapped onto the arterial wall surface. (c) The cross section of the wall and the lumen cut by the slice represented by the black line in (b).

IV. RESULTS

IV.A. Test phantom experiments

We computed the VWT between the arterial wall and the normal artery and show the result in Fig. 10(b) as a color-coded VWT map superimposed on the arterial wall. Ideally, the VWT should be identically 1 mm everywhere on the arterial wall. Figure 12(a) shows the frequency distribution of VWTs calculated at all the vertices of the model, with a bin size of 0.02 mm and centered at 1 mm. This figure shows that $\sim$95% of the vertices on the wall have a thickness ranging from 0.99 to 1.01 mm measured from the normal artery (considered as the arterial lumen here).

The arterial wall and the 30%-stenotic arterial model (referred to as arterial lumen) was shown in Fig. 11(a). Figure 11(b) shows the VWT map, which was color-coded and superimposed on the arterial wall. The VWT map demonstrates the variation in thickness along the stenosed region. Figure 11(b) shows the frequency distribution of VWTs calculated for this model. In order to validate the VWT measurements, we have compared the frequency distribution of VWTs with the "gold standard," which was established by corresponding point pairs obtained by casting rays from each point on the

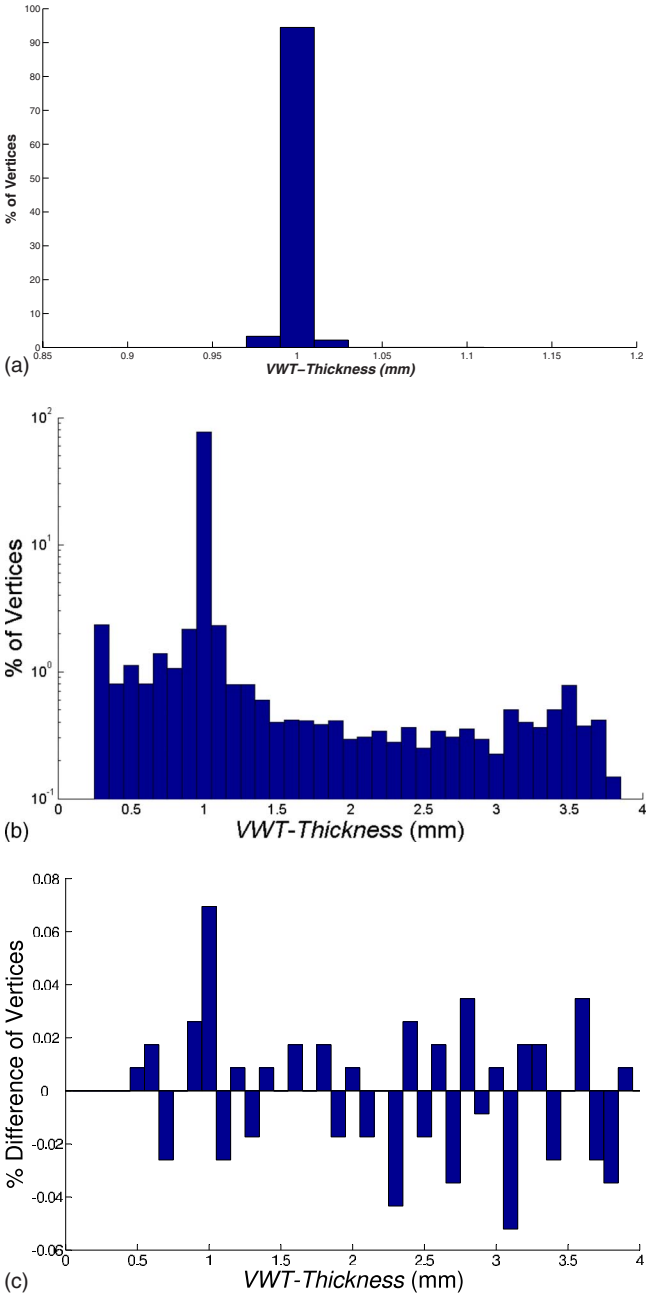

FIG. 12. The frequency distributions of the VWTs between the synthetic arterial wall and (a) the normal arterial model and (b) the 30%-stenotic arterial model. (c) The difference between the distribution shown in (b) and the "gold standard" of the VWT distribution.

arterial wall along the normal direction of the wall, until the ray intersected with the surface of the lumen. This point of intersection was defined as the corresponding point associated with the point on the wall surface from which the ray was cast. The gold standard can be so defined in the phantom study because the wall and lumen contours of the phantom model are either circular or elliptical. In order to show the deviation of the VWT distribution generated by our proposed algorithm from the gold standard, we subtracted the histogram shown in Fig. 12(b) with the VWT distribution gold standard on a bin-by-bin basis. The result is shown in Fig. 12(c), which shows that the VWT distribution obtained and shown in Fig. 12(b) deviates minimally from the gold standard, with the maximum deviation of only 0.07% at the bin centered at 1 mm. The major source of error came from the bifurcation apex as shown in Fig. 11(b). Because of the presence of the stenotic region in the arterial lumen model, the bifurcation of the lumen model was located a few millimeters lower than the bifurcation of the arterial wall model as shown in Fig. 11(a). Thus, there is a mismatch in topology between the cross sections of the wall and lumen when the transverse cutting plane is located between the two bifurcations. An example of such a cutting plane is shown as a black line in Fig. 11(b), and Fig. 11(c) shows the cross sections of the arteries obtained using this cutting plane. Here, the arterial wall cross section is composed of only one closed curve, whereas the cross section of the lumen has two closed curves. Since the symmetric correspondence algorithm can only be used to establish correspondence between two curves with one closed contour, we joined the two closed curves that make up the cross section of the lumen surface [which is represented by the white contours in Fig. 11(c)]. In Fig. 11(c), the white lines join each pair of corresponding points between the arterial wall and the lumen. We observe that there are mismatches near the bifurcation [see Fig. 11(c)]. Symmetric corresponding pairs could not be found at points lying on the blue segment (between points 1 and 2) of the arterial wall contour. The points on the blue segment without a corresponding point were matched with the red segment by (between points 3 and 6) interpolating between the neighboring corresponding pairs [$1\mapsto3$ and $2\mapsto6$ in Fig. 11(c)]. However, the whole blue segment belongs to the ICA and should be matched to the red segment on the left-hand side (between points 3 and 4), which belongs to the ICA. No point should be matched to the red segment on the right-hand side (between points 5 and 6). This mismatch resulted in inaccurate thickness measurements at three points (see points between points 1 and 2).

Fortunately, this type of mismatch only occurs near the bifurcation of two to three cross sections in which the arterial wall and the lumen have different topologies, and affects the accuracy of the thickness measurements at about 10–15 points in total (~0.1% of points on the artery). In addition, the manual segmentation protocol precludes this situation from occurring in the patient data. In our patient study, the expert observer first identified the bifurcation apex. Both the arterial wall and the lumen cross sections consisted of two closed curves when the cutting plane was distal to the bifurcation, and they both consisted of one closed curve when the cutting plane was proximal to the bifurcation.

IV.B. Evaluation using patient 3D US images

IV.B.1. VWT map computation

Figure 13 shows two different views of a meshed lumen and vessel wall surfaces [Figs. 13(a) and 13(c)], as well as the VWT map color-coded and superimposed on the reconstructed vessel wall [Figs. 13(b) and 13(d)], of Subject 1's carotid arteries at base line, who was to be treated with ator-

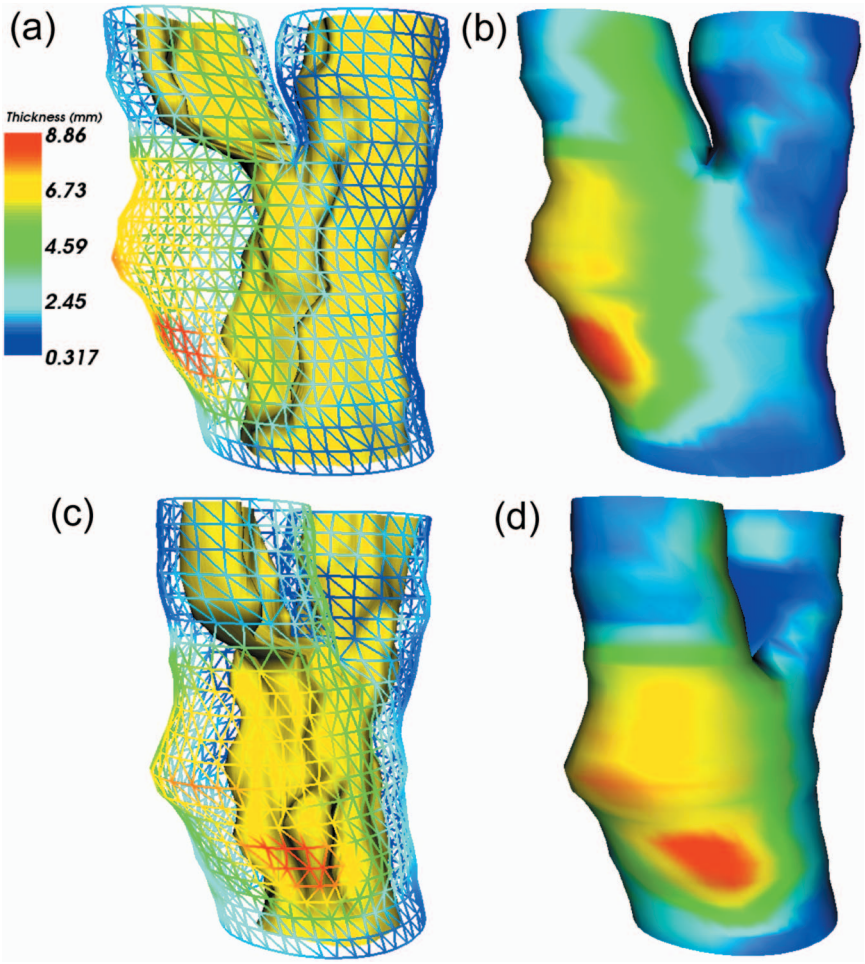

FIG. 13. The VWT map color-coded and superimposed on the vessel wall, and the lumen, of Subject 1. The VWT map is visualized in three views: (a) and (b) The far side of the vessel. (c) and (d) The location where VWT is maximum. (c) The red region on the VWT map (i.e., the region with maximum VWT) corresponds to a deep depression on the lumen surface (i.e., the location of a large plaque).

vastatin. Figures 13(a) and 13(b) show the far side of the vessel (the side further from the US transducer). Figures 13(c) and 13(d) show the location where the VWT is maximum. These views of the VWT map show that the surface correspondence algorithm matches the vessel wall and the lumen surfaces well, which have a much more complicated shape than the phantom used in Sec. IV A. For example, we observe from Figs. 13(c) and 13(d) that the red region on the VWT map (i.e., the region with maximum thickness) corresponds well to a depression in the lumen surface (i.e., the location of a large plaque).

IV.B.2. VWT-Change maps and the results of t-test

Figures 14(a) and 14(e) show the VWT map of Subject 1 in Group 1 at base line (time point 1), and Figs. 14(b) and 14(f) show the VWT map of same subject three months later (time point 2). The top row shows the view on the near side, and the bottom shows the views on the far side from the transducer respectively. Figures 14(c) and 14(g) show the VWT-Change map. The frequency distribution of the VWT-Change values is plotted in Fig. 16(a). Comparing Figs. 14(e) and 14(f) and observing the change shown in Fig. 14(g), we notice that there was a ~7.5 mm change in VWT at the blue region in Fig. 14(g). The results of the point-by-point t-tests are color-coded and superimposed on the arterial wall in Figs. 14(d) and 14(h). In this test, the family-wise error rate, $\hat{\alpha}$, was chosen to be 5% [see Eq. (2)]. Red indicates a statistically significant change (either an increase or decrease) in the VWT, green indicates that there was no statistically significant change, and blue indicates that the test was not performed at that point because the VWT maps at time points 1 and 2 did not overlap. Since the VWT map at time point 2 was reconstructed from fewer slices, the top and bottom slices of the VWT of time point 1 did not correspond to slices of the VWT map of time point 2. We also summarized the results of these tests with two parameters: The percentage of points at which; (1) a significant increase had occurred, and (2) a significant decrease had occurred. For this subject, there were significant decreases in VWT at 11.88% of points tested and significant increases at 1.88% of points. This result could have been estimated from the frequency distribution plotted in Fig. 16(a), which shows that a predominant portion of vertices are associated with negative VWT-Change values.

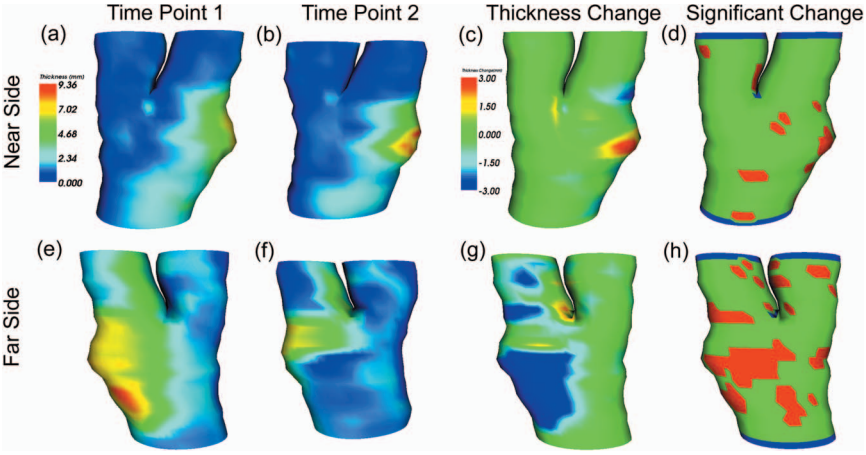

FIG. 14. VWT map, VWT-Change map, and the results of the point-by-point t-tests for Subject 1, who had undergone atorvastatin treatment. (a)–(d) The maps viewed on the near side and (e)–(h) the maps on the far side from the US transducer. (a),(e) the VWT map at time point 1 (base line). (b),(f) The VWT map at time point 2 (3 months after base line). (c),(g) The VWT-Change map. (d),(h) The results of the point-by-point t-tests. Red indicates a significant change, either a significant increase or decrease of thickness, green indicates that there is no significant change, and blue indicates that the test is not performed at that point because the thickness maps at time point 1 and 2 do not overlap.

Figure 15 shows the VWT maps at two time points separated by 2 weeks, VWT-Change map, and the results of the point-by-point t-tests for Subject 4 in Group 2. Figure 15 is arranged in the same way as Fig. 14. The VWT-Change map and the t-tests indicate that the differences in the VWT calculated from images acquired at the two time points (2 weeks apart) are minimal, which agrees with the initial expectation. Figure 16(d) shows the frequency distribution of the VWT-Change values, which are small (with maximum magnitude $\leqslant$0.8 mm) and are symmetrically distributed about 0.

IV.B.3. Comparison between the results generated for Group 1 and Group 2

We used the mean VWT-Change as a global quantification metric to allow a comparison between the plaque burden changes between subjects in Group 1 and Group 2. With this metric, we are able to show that the amount of plaque changes was much more significant in subjects with treatment (i.e., Group 1) than those without (i.e., Group 2). Table I shows the mean VWT at two time points and the mean VWT-Change for the six subjects. These means were computed by averaging the VWT (or VWT-Change) values at all points at which correspondence pairs between the arterial wall surfaces associated with time points 1 and 2 exist (i.e., points lying on slices on which VWT maps at time points 1 and 2 do not overlap were not included).

As a validation, we compare the mean VWT-Change with the VWV change measured using the technique described by Egger *et al.*[52] The mean VWT-Change and the VWV-Change are closely related. VWV change is approximately equal to

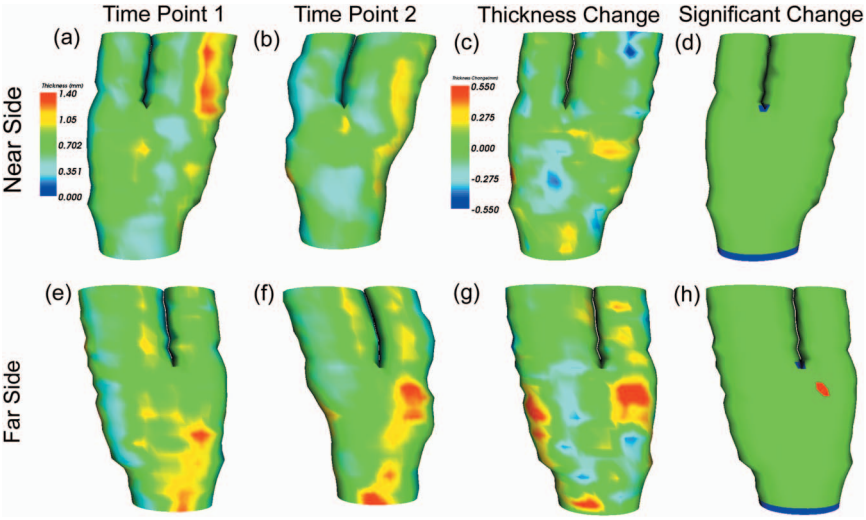

FIG. 15. VWT map, VWT-Change map, and the results of the point-by-point t-tests for Subject 4 with no treatment administered. The figure is arranged in the same way as Fig. 14.

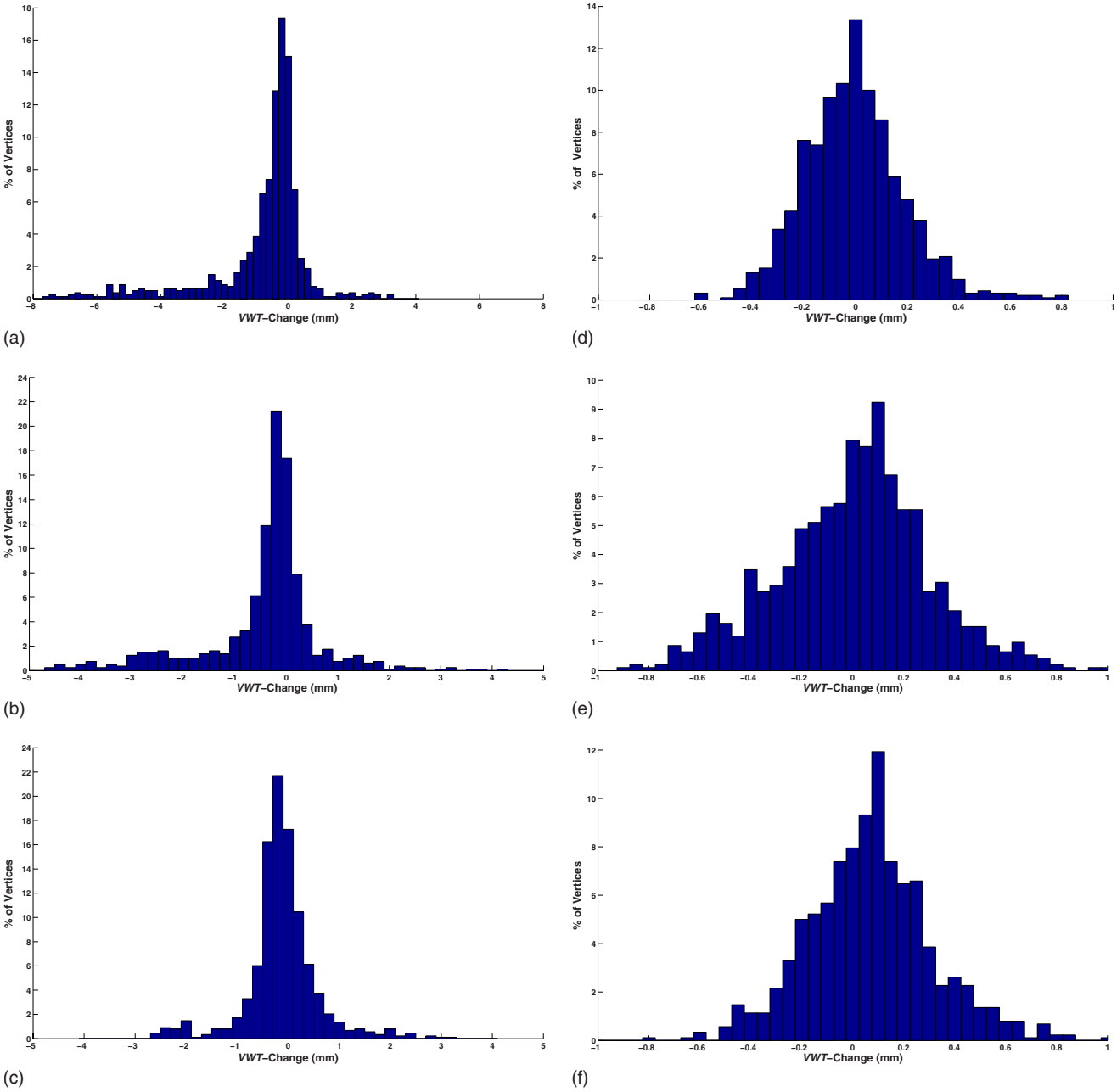

FIG. 16. Frequency distribution of the VWT-Changes for six subjects. (a)–(c) The VWT-Changes distribution for Subjects 1 to 3, respectively, who had been treated by atrovastatin. The VWT-Changes range from −8 to 8, −6 to 6, and −5 to 5 mm in (a), (b), and (c), respectively. (d)–(f) The VWT-Changes distribution for Subjects 4 to 6, respectively, who had not received any treatment. The VWT-Changes range from −1 to 1 mm in (d) to (f).

VWT-Change integrated over the whole surface of the vessel wall. Thus, the mean of VWT-Change at all points can be interpreted as a scaled approximation of the VWV-Change. Table II shows the VWV obtained for the six subjects at time points 1 and 2, and the VWV changes. We found that the mean VWT-Change measurements tabulated in the last column of Table I are consistent with the VWV-Change measurements tabulated in the last column of Table II. Both the mean VWT-Change and the VWV change show that the largest change occurred in Subject 1, followed by Subjects 2 and 3, in that order, while both metrics show the changes that occurred in the three subjects of Group 2 are small.

Figures 16(a)–16(c) show the distribution of VWT-Changes for Subjects 1 to 3, respectively, and Figs. 16(d)–16(f) show the distribution of VWT-Changes for Subjects 4 to 6, respectively. Table III summarizes the results of the point-by-point t-tests.

For the three subjects under atorvastatin treatments, the mean VWT-Changes were negative, and the percentages of points with statistically significant VWT decrease were five to ten times greater than those with VWT increase, which suggested that regression of plaque burden had occurred in these subjects. Among these three subjects, the mean VWT-Change and the percentage of points with statistically signifi-

TABLE I. Mean VWT and VWT-Change for six subjects. The first and the Second column, show the 95% confidence intervals (CI) of the mean of the VWT map generated for the carotid images acquired at the first and the second time points, respectively. The third column shows the 95% CIs of the VWT-Change.

		Mean VWT and the 95% CI (mm)		Mean VWT-Change and the 95% CI (mm)
	Subject	Time point 1	Time point 2	
With treatment	1	2.45 (2.31–2.59)	1.69 (1.58–1.80)	−0.76(−0.87–−0.65)
	2	1.43 (1.35–1.51)	1.03 (0.97–1.10)	−0.40(−0.48–−0.32)
	3	1.07 (1.03–1.12)	0.95 (0.90–1.00)	−0.12(−0.17–−0.07)
Without treatment	4	0.67 (0.66–0.69)	0.66 (0.65–0.68)	−0.01(−0.02–0.00)
	5	0.84 (0.82–0.86)	0.84 (0.82–0.85)	0.00(−0.02–0.02)
	6	0.79 (0.77–0.82)	0.86 (0.83–0.88)	0.07(0.05–0.08)

cant VWT decrease suggested that the regression was the largest in Subject 1 and the smallest in Subject 3, which agrees with the results obtained in Ainsworth's study,[34] where plaque volumes were measured.

The mean VWT-Changes for the group of subjects without treatment were very close to 0, indicating the *vessel-wall-plus-plaque* volume changes were very small. The percentages of points with statistically significant VWT-Changes were negligible for Subjects 4 and 5, where those associated with Subject 6 suggested an increase of VWT in a very small region.

V. DISCUSSION AND CONCLUSION

In this paper, we demonstrated the calculation of a point-by-point VWT map of the carotid arteries using 3D US images. Performing a point-by-point measurement of the VWT is difficult mainly because there is a need to define a correspondence mapping between the arterial wall and the lumen, and the establishment of such correspondence map is nontrivial, which is further complicated by the irregularity of the carotid lumen boundary of an atherosclerotic patient. Several methods have been proposed to measure point-by-point vessel wall thickness in MRI. Underhill *et al.*[66] matched a point on the lumen contour with a point on the outer wall that is closest to it. They ensured one-to-one matching between points by removing a point from the outer wall after it has been matched with one on the lumen contour. One problem of this thickness computation method is that the accuracy of the thickness depends on the sampling interval of the contours, and the thickness would be significantly overestimated if the contours are sparsely sampled and relatively displaced as discussed in Yezzi *et al.*[67] Mani *et al.*[68] determined carotid arterial thickness in MR cross-sectional images by matching points on the outer and inner wall that intersect the same radial line drawn from a manually identified center point. This method depends on the position of the manually identified center point. In addition, the thickness would be overestimated if the normal of the wall boundaries deviate significantly from the direction of the radial line. Boussel *et al.*[69] first determined a central axis or a skeleton that is equidistant from the wall and the lumen boundaries. Then, the local wall thickness was computed at regularly spaced locations along the central axis by measuring the distance between the lumen and the wall boundaries in the direction perpendicular to the central axis. Yezzi *et al.*[67] has pointed out a few problems with this method. One problem is that the central axis will take on an arbitrary topology in order to describe highly convoluted objects. In addition, it may be possible that the line perpendicular to the central axis does not have an intersection with the lumen or the wall boundaries, in which case the thickness would be undefined. Our modified symmetric correspondence algorithm does not depend on a center point or a central axis, and thus not subject to the problems associated with the algorithms by Mani *et al.*[68] and Boussel *et al.*[69] It is, however, subject to the limitation of Underhill's[66] algorithm when computing the symmetric correspondence pairs. However, unlike the algorithm proposed by Underhill *et al.*,[66] the proposed algorithm

TABLE II. Vessel-wall-plus-plaque volume (VWV) of the six subjects at the first and the second scanning sessions and VWV-Change. Age and sex of the subjects are also listed.

				Vessel-wall-plus-plaque volume (VWV) (mm^3)		
Subject		Age	Sex	Time point 1	Time point 2	VWV-Change (mm^3)
With treatment	1	72	M	1570	1122	−448
	2	74	M	993	714	−279
	3	63	F	770	670	−100
Without treatment	4	76	F	571	532	−39
	5	58	M	804	770	−34
	6	76	M	627	672	45

TABLE III. The first two columns show the percentages of points on the arterial wall that have undergone a statistically significant increase, decrease on the VWT during the interval between the first and the second acquisitions. The third column shows the total percentage of points with statistically significant changes.

		% of points with statistically significant change		
	Subject	Increase	Decrease	Total
With treatment	1	1.88	11.88	13.75
	2	1.50	10.00	11.50
	3	1.14	5.34	6.47
Without treatment	4	0.11	0.00	0.11
	5	0.65	0.00	0.65
	6	1.02	0.11	1.13

matches only symmetric nearest neighbors and, therefore, would not match two vertices with significant relative displacement.

Although there is no universal consensus on which surface (or curve in 2D) correspondence mapping is the best, we showed that the modified symmetric correspondence algorithm gave accurate VWT measurements in the phantom experiments (Sec. IV A), and reasonable VWT measurements in the patient evaluation (Sec. IV B).

However, our surface correspondence algorithm is not without its limitations. We chose to use reslicing planes that are perpendicular to the mean longitudinal axis of the CCA (obtained by averaging five repeated choices from the expert observer) along the arteries. However, if the direction of the ICA or ECA branch immediately distal to the bifurcation deviates from the direction of the longitudinal axis of the CCA, it would be more appropriate to select a plane that is perpendicular to the branch for reslicing. Since the reslicing plane we use is not perpendicular to the ICA or ECA branch in this case, an overestimation of VWT would occur, which we have not taken into account in this study. However, defining slicing planes that are perpendicular to the vessel surface would involve determining the centerline of the vessel. First, although algorithms are available for determining centerline of carotid vessels segmented from MR and CT images,[70,71] they may not be suitable for the noisier nature of the arterial surfaces segmented from US images (see Figs. 3, 14, and 15). Although the carotid wall surfaces could be smoothened by aligning the centroids of the cross-sectional contours before the centerline is produced,[38,72] smoothing is not preferred because the geometry of the carotid arteries may not be faithfully represented after smoothing. The problem of unmatched correspondence (and, equivalently, incorrect estimation of VWT) would be much more pronounced if we defined the reslicing plane based to a noisy centerline. Second, for a branched surface such as the carotid vessel, the centerline starts to branch at a point that is proximal to the bifurcation.[70] In this case, the reslicing plane, and therefore the thickness, at the region of the CCA that is proximal to the vessel bifurcation, but distal to the centerline branching point, would be undefined. Finally, the main focus of the proposed algorithm is to monitor changes of VWT. Thus, even if the thickness were overestimated at the carotid bulb when either the ICA or ECA branch immediately distal to the bifurcation deviates from the longitudinal axis, this overestimation would be canceled when calculating the thickness change. However, it is important to notice that we did not find a significant overestimation of VWT in our experiments with clinical data, because there was no significant angular deviation between the direction of the ICA or ECA segment immediately distal to the bifurcation and the longitudinal axis of the CCA in the subjects we investigated in this study (see Figs. 3, 14, and 15).

We performed a point-by-point statistical comparison between the VWT maps computed at two different time points for six subjects. Using 3D US images acquired for six subjects (Sec. IV B), we demonstrated that: (a) the spatial distribution of VWT-Changes in the carotid arteries can be calculated and displayed, as demonstrated by the results obtained for the three subjects receiving the atorvastatin treatment compared to that of the three subjects who had not received any treatment; (b) the mean of VWT-Change at all points can be interpreted as a scaled approximation of the VWV-Change (vessel-wall-volume-change) and, therefore, in addition to providing a 3D distribution of vessel wall thickness change, our method can also be used in obtaining an estimate of change in total plaque burden; and (c) the VWT-Change maps and the variances in the segmentation of the vessel and lumen boundaries can be used to test whether the observed changes in local VWT are statistically significant.

The statistical comparison is useful in determining whether or not the VWT-Change is mainly attributable to the intraobserver variability in manual segmentations. In this study, we used the Bonferroni method to control the family-wise error rate at level $\hat{\alpha}$. It is commonly known that the Bonferroni method is overly conservative, especially when the test statistics are not independent, which applies to our study because the VWT measurements at neighboring points are not independent. As a result, the power (i.e., the fraction of true differences the test identifies) is low. There are a number of ways to increase the power of our statistical tests. First, we often want to draw a conclusion about the VWT change in a diseased region, instead of the whole artery. In this case, we should include only the points that are within the diseased region, instead of all points on the artery, thereby reducing N in Eq. (2), increasing the per-comparison error rate α and the power. Second, "improved Bonferroni procedures," such as Hochberg's procedure,[73] can be adopted to increase the power, while controlling the family-wise error rate at the same level. Further increase in power can be achieved by controlling the false discovery rate (FDR). Instead of controlling the probability of erroneously rejecting even one true null hypothesis (the family-wise error rate), Benjamini *et al.*[74] proposed controlling the FDR, which is defined as the expected proportion of rejected null hypotheses that are erroneously rejected. They showed that there is a large power gain if FDR is controlled, instead of the family-wise error rate. A further modification of the method

by Benjamini *et al.*[74] allows controlling FDR when the test statistics (VWTs in our case) are dependent.[75]

In our proposed statistical study in VWT-Change, we did not include interobserver variability. Landry *et al.*[76] reported that the interobserver standard deviation in detection of the plaque boundary contours is approximately a factor of 2 higher than the intraobserver standard deviation. Since our focus here is to develop a sensitive tool in detecting statistically significant change in VWT, a lower variability in detecting the arterial wall and lumen was desirable as the minimum detectable change equals approximately to $(z_{\alpha/2}+z_{\beta})$ s.e., where s.e. is computed using Eq. (4), which is a function of the variances of the arterial wall and lumen segmentation in time points 1 and 2, and $z_{\alpha/2}$ and z_{β} depend on the level of significance and power used, respectively (e.g., $z_{\alpha/2}=1.96$ and $z_{\beta}=0.84$ correspond to a power of 80% and a significant level of 5%). Although the use of repeated segmentations of one observer may be subject to bias, the effect of observer bias is not significant in computing VWT-Change since the bias would likely be canceled when computing the change.

The intraobserver variability in the segmentation protocol can be separated into the two components: (1) the variability due to the choice of the longitudinal axis (equivalently, the choice of transverse reslicing plane), and (2) the variability in segmenting 2D resliced images. Although the VWT maps obtained at time points 1 and 2 have been registered, the orientations of the longitudinal axes in the two maps would be slightly different because of operator variability, which may have an effect in the VWT measurements. Thus, our inclusion of the first component of intraobserver variability in VWT is necessary, although it is possible to eliminate it by choosing the axis once and use it in all five segmentation sessions of a 3D image. However, a future study focusing on obtaining the fractional contribution of the variability due to the axis choice is useful in assessing whether this variability is sufficiently large to warrant the longer time spent in choosing the longitudinal axis in each segmentation session over choosing the axis once and using it for all sessions.

We would point out that our method does not account for errors in registration that may be caused by: (1) distortions in the geometry of the carotid arteries caused by different head positions during the two imaging sessions; (2) distortions in the vessel wall caused by cardiac pulsation; and (3) different contrast and brightness in the acquired US images at the two sessions, which resulted in a possible segmentation bias. Although these effects were observed to be small as demonstrated in the results obtained for the three subjects in Group 2 [who had not received any medical treatment and were imaged two weeks apart (Sec. IV B 3)], improvements corresponding to the above-presented three issues can be implemented in future studies: (1) Effect of distortions in the carotid arteries due to different head orientations can be minimized by a nonrigid registration technique.[77] (2) Distortions due to cardiac pulsation can be minimized by acquiring the 3D US images using the cardiac gating techniques;[78] however, this will lengthen the scan time, increasing the susceptibility to involuntary patient head motion and swallowing. (3) Contrast and brightness variations in the images can be minimized by standardizing the acquisition "time-gain control" settings of the US machine.

In this paper, we evaluated our algorithm using six subjects, three were treated with atorvastatin therapy and three were not. Future studies involving a large number of subjects are now ongoing, in which the proposed VWT and VWT-Change maps will be used. Although a clinical trial is required to demonstrate whether any treatment provides a significant benefit, we showed that the proposed quantitative metrics can assist in monitoring localized regression in carotid plaques in patients using 3D US images, and can be used in clinical trials to obtain more detailed information on the spatial distribution of carotid plaque progression and regression.

ACKNOWLEDGMENTS

The authors would like to thank J. Milner and D. W. Holdsworth for providing the phantom models for this study. The authors gratefully acknowledge the financial support provided by the Canadian Institute of Health Research. A.F. holds a Canada Research Chair in Biomedical Engineering, and acknowledges the support of the Canada Research Chair Program. B.C. acknowledges the support of the Ontario Graduate Scholarship.

[a]Electronic mail: bchiu@imaging.robarts.ca

[1]T. Thom, N. Haase, W. Rosamond, V. J. Howard, J. Rumsfeld, T. Manolio, Z. J. Zheng, K. Flegal, C. O'Donnell, S. Kittner, D. Lloyd-Jones, D. C. Goff, Jr., Y. Hong, R. Adams, G. Friday, K. Furie, P. Gorelick, B. Kissela, J. Marler, J. Meigs, V. Roger, S. Sidney, P. Sorlie, J. Steinberger, S. Wasserthiel-Smoller, M. Wilson, P. Wolf, and the American Heart Association Statistics Committee and Stroke Statistics Subcommittee, "Heart disease and stroke statistics—2006 update: A report from the American Heart Association Statistics Committee and Stroke Statistics Subcommittee," Circulation **113**, e85–151 (2006).
[2]B. M. Eicke, J. von Lorentz, and W. Paulus, "Embolus detection in different degrees of carotid disease," Neurol. Res. **17**, 181–184 (1995).
[3]J. Golledge, R. M. Greenhalgh, and A. H. Davis, "The symptomatic carotid plaque," Stroke **31**, 774–781 (2000).
[4]P. B. Gorelick, "Stroke prevention. An opportunity for efficient utilization of health care resources during the coming decade," Stroke **25**, 220–224 (1994).
[5]J. D. Spence, "Intensive management of risk factors for accelerated atherosclerosis: The role of multiple interventions," Curr. Neurol. Neurosci. Rep. **7**, 42–48 (2007).
[6]P. Libby and M. Aikawa, "Stabilization of atherosclerotic plaques: New mechanisms and clinical targets," Nat. Med. (N.Y.) **8**, 1257–1262 (2002).
[7]V. Fuster, *The Vulnerable Atherosclerotic Plaque: Understanding, Identification, and Modification* (Futura, Armonk, NY, 1999).
[8]N. Nighoghossian, L. Derex, and P. Douek, "The vulnerable carotid artery plaque: Current imaging methods and new perspectives," Stroke **36**, 2764–2772 (2005).
[9]J. A. Lima, M. Y. Desai, H. Steen, W. P. Warren, S. Gautam, and S. Lai, "Statin-induced cholesterol lowering and plaque regression after 6 months of magnetic resonance imaging-monitored therapy," Circulation **110**, 2336–2341 (2004).
[10]C. Yuan, L. M. Mitsumori, K. W. Beach, and K. R. Maravilla, "Carotid atherosclerotic plaque: Noninvasive MR characterization and identification of vulnerable lesions," Radiology **221**, 285–299 (2001).
[11]B. A. Wasserman, W. I. Smith, H. H. Trout III, R. O. Cannon III, R. S. Balaban, and A. E. Arai, "Carotid artery atherosclerosis: In Vivo morphologic characterization with gadolinium-enhanced double-oblique MR imaging initial results," Radiology **223**, 566–573 (2002).
[12]W. Kerwin, A. Hooker, M. Spilker, P. Vicini, M. Ferguson, T. Hatsukami, and C. Yuan, "Quantitative magnetic resonance imaging analysis of

neovasculature volume in carotid atherosclerotic plaque," Circulation **107**, 851–856 (2003).
[13]C. Yuan, K. W. Beach, L. H. Smith, Jr., and T. S. Hatsukami, "Measurement of atherosclerotic carotid plaque size in vivo using high resolution magnetic resonance imaging," Circulation **98**, 2666–2671 (1998).
[14]X. Kang, N. L. Polissar, C. Han, E. Lin, and C. Yuan, "Analysis of the measurement precision of arterial lumen and wall areas using high-resolution MRI," Magn. Reson. Med. **44**, 968–972 (2000).
[15]S. Zhang, T. S. Hatsukami, N. L. Polissar, C. Han, and C. Yuan, "Comparison of carotid vessel wall area measurements using three different contrast-weighted black blood MR imaging techniques," Magn. Reson. Imaging **19**, 795–802 (2001).
[16]T. S. Hatsukami, R. Ross, N. L. Polissar, and C. Yuan, "Visualization of fibrous cap thickness and rupture in human atherosclerotic carotid plaque in vivo with high-resolution magnetic resonance imaging," Circulation **102**, 959–964 (2000).
[17]L. M. Mitsumori, T. S. Hatsukami, M. S. Ferguson, W. S. Kerwin, J. Cai, and C. Yuan, "In vivo accuracy of multisequence MR imaging for identifying unstable fibrous caps in advanced human carotid plaques," J. Magn. Reson Imaging **17**, 410–420 (2003).
[18]C. Yuan, S. X. Zhang, N. L. Polissar, D. Echelard, G. Ortiz, J. W. Davis, E. Ellington, M. S. Ferguson, and T. S. Hatsukami, "Identification of fibrous cap rupture with magnetic resonance imaging is highly associated with recent transient ischemic attack or stroke," Circulation **105**, 181–185 (2002).
[19]M. Shinnar, J. T. Fallon, S. Wehrli, M. Levin, D. Dalmacy, Z. A. Fayad, J. J. Badimon, M. Harrington, E. Harrington, and V. Fuster, "The diagnostic accuracy of ex vivo MRI for human atherosclerotic plaque characterization," Arterioscler., Thromb., Vasc. Biol. **19**, 2756–2761 (1999).
[20]C. Yuan, L. M. Mitsumori, M. S. Ferguson, N. L. Polissar, D. Echelard, G. Ortiz, R. Small, J. W. Davies, W. S. Kerwin, and T. S. Hatsukami, "In vivo accuracy of multispectral magnetic resonance imaging for identifying lipid-rich necrotic cores and intraplaque hemorrhage in advanced human carotid plaques," Circulation **104**, 2051–2056 (2001).
[21]J. M. Cai, T. S. Hatsukami, M. S. Ferguson, R. Small, N. L. Polissar, and C. Yuan, "Classification of human carotid atherosclerotic lesions with in vivo multicontrast magnetic resonance imaging," Circulation **106**, 1368–1373 (2002).
[22]C. Yuan, W. S. Kerwin, M. S. Ferguson, N. Polissar, S. Zhang, J. Cai, and T. S. Hatsukami, "Contrast-enhanced high resolution MRI for atherosclerotic carotid artery tissue characterization," J. Magn. Reson Imaging **15**, 62–67 (2002).
[23]W. S. Kerwin, K. D. O'Brien, M. S. Ferguson, N. Polissar, T. S. Hatsukami, and C. Yuan, "Inflammation in carotid atherosclerotic plaque: A dynamic contrast-enhanced MR imaging study," Radiology **241**, 459–468 (2006).
[24]T. Leiner, S. Gerretsen, R. Botnar, E. Lutgens, V. Cappendijk, E. Kooi, and J. van Engelshoven, "Magnetic resonance imaging of atherosclerosis," Eur. Radiol. **15**, 1087–1099 (2005).
[25]A. Berg, J. Sailer, T. Rand, and E. Moser, "Diffusivity- and T2 imaging at 3 tesla for the detection of degenerative changes in human-excised tissue with high resolution: Atherosclerotic arteries," Invest. Radiol. **38**, 452–459 (2003).
[26]H. K. Song, A. C. Wright, R. L. Wolf, and F. W. Wehrli, "Multislice double inversion pulse sequence for efficient black-blood MRI," Magn. Reson. Med. **47**, 616–620 (2002).
[27]C. Yuan and W. S. Kerwin, "MRI of atherosclerosis," J. Magn. Reson Imaging **19**, 710–719 (2004).
[28]M. G. Hunink, J. F. Polak, M. M. Barlan, and D. H. O'Leary, "Detection and quantification of carotid artery stenosis: Efficacy of various Doppler velocity parameters," AJR, Am. J. Roentgenol. **160**, 619–625 (1993).
[29]A. Fenster, D. B. Downey, and H. N. Cardinal, "Three-dimensional ultrasound imaging," Phys. Med. Biol. **46**, R67–99 (2001).
[30]S. Meairs, J. Beyer, and M. Hennerici, "Reconstruction and visualization of irregularly sampled three-and four-dimensional ultrasound data for cerebrovascular applications," Ultrasound Med. Biol. **26**, 263–272 (2000).
[31]J. A. Hossack, T. S. Sumanaweera, S. Napel, and J. S. Ha, "Quantitative 3-d diagnostic ultrasound imaging using a modified transducer array and an automated image tracking technique," IEEE Trans. Ultrason. Ferroelectr. Freq. Control **49**, 1029–1038 (2002).
[32]C. P. Allott, C. D. Barry, R. Pickford, and J. C. Waterton, "Volumetric assessment of carotid artery bifurcation using freehand-acquired, compound 3D ultrasound," Br. J. Radiol. **72**, 289–292 (1999).
[33]J. D. Spence, M. Eliasziw, M. DiCicco, D. G. Hackam, R. Galil, and T. Lohmann, "Carotid plaque area: A tool for targeting and evaluating vascular preventive therapy," Stroke **33**, 2916–2922 (2002).
[34]C. D. Ainsworth, C. C. Blake, A. Tamayo, V. Beletsky, A. Fenster, and J. D. Spence, "3D ultrasound measurement of change in carotid plaque volume: A tool for rapid evaluation of new therapies," Stroke **36**, 1904–1909 (2005).
[35]C. Liapis, J. Kakisis, V. Papavassiliou, A. Ntanou, S. Kontopoulou, E. Kaperonis, K. Koumakis, and J. Gogas, "Internal carotid artery stenosis: Rate of progression," Eur. J. Vasc. Endovasc Surg. **19**, 111–117 (2000).
[36]R. A. Markus, W. J. Mack, S. P. Azen, and H. N. Hodis, "Influence of lifestyle modification on atherosclerotic progression determined by ultrasonographic change in the common carotid intima-media thickness," Am. J. Clin. Nutr. **65**, 1000–1004 (1997).
[37]J. M. Seeger, E. Barratt, G. A. Lawson, and N. Klingman, "The relationship between carotid plaque composition, plaque morphology, and neurologic symptoms," J. Surg. Res. **58**, 330–336 (1995).
[38]D. C. Barratt, B. B. Ariff, K. N. Humphries, S. A. Thom, and A. D. Hughes, "Reconstruction and quantification of the carotid artery bifurcation from 3-D ultrasound images," IEEE Trans. Med. Imaging **23**, 567–583 (2004).
[39]A. Landry, J. D. Spence, and A. Fenster, "Measurement of carotid plaque volume by 3-dimensional ultrasound," Stroke **35**, 864–869 (2004).
[40]J. Yao, M. R. van Sambeek, A. Dall'Agata, L. C. van Dijk, M. Kozakova, P. J. Koudstaal, and J. R. Roelandt, "Three-dimensional ultrasound study of carotid arteries before and after endarterectomy; analysis of stenotic lesions and surgical impact on the vessel," Stroke **29**, 2026–2031 (1998).
[41]U. Schminke, L. Motsch, L. Hilker, and C. Kessler, "Three-dimensional ultrasound observation of carotid artery plaque ulceration," Stroke **31**, 1651–1655 (2000).
[42]S. Meairs and M. Hennerici, "Four-dimensional ultrasonographic characterization of plaque surface motion in patients with symptomatic and asymptomatic carotid artery stenosis," Stroke **30**, 1807–1813 (1999).
[43]Y. Luo, N. Polissar, C. Han, V. Yarnykh, W. S. Kerwin, T. S. Hatsukami, and C. Yuan, "Accuracy and uniqueness of three in vivo measurements of atherosclerotic carotid plaque morphology with black blood MRI," Magn. Reson. Med. **50**, 75–82 (2003).
[44]R. F. Smith, B. K. Rutt, A. J. Fox, R. N. Rankin, and D. W. Holdsworth, "Geometric characterization of stenosed human carotid arteries," Acad. Radiol. **3**, 898–911 (1996).
[45]J. D. Gill, H. M. Ladak, D. A. Steinman, and A. Fenster, "Accuracy and variability assessment of a semiautomatic technique for segmentation of the carotid arteries from three-dimensional ultrasound images," Med. Phys. **27**, 1333–1342 (2000).
[46]P. J. Touboul, M. G. Hennerici, S. Meairs, H. Adams, P. Amarenco, N. Bornstein, L. Csiba, M. Desvarieux, S. Ebrahim, M. Fatar, R. Hernandez, M. Jaff, S. Kownator, P. Prati, T. Rundek, M. Sitzer, U. Schminke, J. C. Tardif, A. Taylor, E. Vicaut, K. S. Woo, F. Zannad, and M. Zureik, "Mannheim carotid intima-media thickness consensus (2004–2006). An update on behalf of the Advisory Board of the 3rd and 4th Watching the Risk Symposium, 13th and 15th European Stroke Conferences, Mannheim, Germany, 2004, and Brussels, Belgium, 2006," Cerebrovasc Dis. **23**, 75–80 (2007).
[47]G. Schulte-Altedorneburg, D. W. Droste, S. Felszeghy, M. Kellermann, V. Popa, K. Hegedus, C. Hegedus, M. Schmid, L. Modis, E. B. Ringelstein, and L. Csiba, "Accuracy of in vivo carotid B-mode ultrasound compared with pathological analysis: Intima-media thickening, lumen diameter, and cross-sectional area," Stroke **32**, 1520–1524 (2001).
[48]M. Wong, J. Edelstein, J. Wollman, and M. G. Bond, "Ultrasonic-pathological comparison of the human arterial wall. Verification of intima-media thickness," Arterioscler. Thromb. **13**, 482–486 (1993).
[49]J. Persson, J. Formgren, B. Israelsson, and G. Berglund, "Ultrasound-determined intima-media thickness and atherosclerosis. Direct and indirect validation," Arterioscler. Thromb. **14**, 261–264 (1994).
[50]P. Pignoli, E. Tremoli, A. Poli, P. Oreste, and R. Paoletti, "Intimal plus medial thickness of the arterial wall: A direct measurement with ultrasound imaging," Circulation **74**, 1399–1406 (1986).
[51]P. A. Barnett, J. D. Spence, S. B. Manuck, and J. R. Jennings, "Psychological stress and the progression of carotid artery disease," J. Hypertens. **15**, 49–55 (1997).
[52]M. Egger, J. D. Spence, A. Fenster, and G. Parraga, "Validation of 3D ultrasound vessel wall volume: An imaging phenotype of carotid athero-

sclerosis," Ultrasound Med. Biol. **33**, 905–914 (2007).
[53]X. Papademetris, A. J. Sinusas, D. P. Dione, R. T. Constable, and J. S. Duncan, "Estimation of 3-D left ventricular deformation from medical images using biomechanical models," IEEE Trans. Med. Imaging **21**, 786–800 (2002).
[54]I. Cohen, N. Ayache, and P. Sulger, "Tracking points on deformable objects using curvature information," *Proceedings of the Second European Conference on Computer Vision*, Santa Margherita Ligure, Italy, May 19–22, 1992.
[55]H. D. Tagare, "Shape-based nonrigid correspondence with application to heart motion analysis," IEEE Trans. Med. Imaging **18**, 570–579 (1999).
[56]P. J. Besl and N. D. McKay, "A method for registration of 3-D shapes," IEEE Trans. Pattern Anal. Mach. Intell. **14**, 239–256 (1992).
[57]H. M. Ladak, F. Mao, Y. Wang, D. B. Downey, D. A. Steinman, and A. Fenster, "Prostate boundary segmentation from 2D ultrasound images," Med. Phys. **27**, 1777–1788 (2000).
[58]H. Motulsky, *Intuitive Biostatistics* (Oxford University Press, New York, 1995).
[59]J. M. Bland and D. G. Altman, "Multiple significance tests: The Bonferroni method," BMJ **310**, 170 (1995).
[60]F. E. Satterthwaite, "An approximate distribution of estimates of variance components," Biomet. Bull. **2**, 110–114 (1946).
[61]T. Kawasaki, S. Sasayama, S. Yagi, T. Asakawa, and T. Hirai, "Non-invasive assessment of the age related changes in stiffness of major branches of the human arteries," Cardiovasc. Res. **21**, 678–687 (1987).
[62]A. R. Ahlgren, F. Hansen, B. Sonesson, and T. Lanne, "Stiffness and diameter of the common carotid artery and abdominal aorta in women," Ultrasound Med. Biol. **23**, 983–988 (1997).
[63]N. M. van Popele, D. E. Grobbee, M. L. Bots, R. Asmar, J. Topouchian, R. S. Reneman, A. P. Hoeks, D. A. van der Kuip, A. Hofman, and J. C. Witteman, "Association between arterial stiffness and atherosclerosis: The Rotterdam study," Stroke **32**, 454–460 (2001).
[64]H. N. Cardinal, J. D. Gill, and A. Fenster, "Analysis of geometrical distortion and statistical variance in length, area, and volume in a linearly scanned 3-D ultrasound image," IEEE Trans. Med. Imaging **19**, 632–651 (2000).
[65]A. Fenster, A. Landry, D. B. Downey, R. A. Hegele, and J. D. Spence, "3D ultrasound imaging of the carotid arteries," Curr. Drug Targets Cardiovasc. Haematol. Disord. **4**, 161–175 (2004).
[66]H. R. Underhill, W. S. Kerwin, T. S. Hatsukami, and C. Yuan, "Automated measurement of mean wall thickness in the common carotid artery by MRI: A comparison to intima-media thickness by B-mode ultrasound," J. Magn. Reson Imaging **24**, 379–387 (2006).
[67]A. J. Yezzi, Jr. and J. L. Prince, "An Eulerian PDE approach for computing tissue thickness," IEEE Trans. Med. Imaging **22**, 1332–1339 (2003).
[68]V. Mani, S. H. Aguiar, V. V. Itskovich, K. B. Weinshelbaum, J. E. Postley, E. J. Wasenda, J. G. Aguinaldo, D. D. Samber, and Z. A. Fayad, "Carotid black blood MRI burden of atherosclerotic disease assessment correlates with ultrasound intima-media thickness," J. Cardiovasc. Magn. Reson. **8**, 529–534 (2006).
[69]L. Boussel, A. Serusclat, M. R. Skilton, F. Vincent, S. Bernard, P. Moulin, D. Saloner, and P. C. Douek, "The reliability of high resolution MRI in the measurement of early stage carotid wall thickening," J. Cardiovasc. Magn. Reson. **9**, 771–776 (2007).
[70]L. Antiga and D. A. Steinman, "Robust and objective decomposition and mapping of bifurcating vessels," IEEE Trans. Med. Imaging **23**, 704–713 (2004).
[71]L. Antiga, B. Ene-Iordache, and A. Remuzzi, "Computational geometry for patient-specific reconstruction and meshing of blood vessels from MR and CT angiography," IEEE Trans. Med. Imaging **22**, 674–684 (2003).
[72]F. P. Glor, B. Ariff, L. A. Crowe, A. D. Hughes, P. L. Cheong, S. A. Thom, P. R. Verdonck, D. N. Firmin, D. C. Barratt, and X. Y. Xu, "Carotid geometry reconstruction: A comparison between MRI and ultrasound," Med. Phys. **30**, 3251–3261 (2003).
[73]Y. Hochberg, "A sharper Bonferroni procedure for multiple tests of significance," Biometrika **75**, 800–802 (1988).
[74]Y. Benjamini and Y. Hochberg, "Controlling the false discovery rate: A practical and powerful approach to multiple testing," J. R. Stat. Soc. Ser. B (Methodol.) **57**, 289–300 (1995).
[75]Y. Benjamini and D. Yekutieli, "The control of the false discovery rate in multiple testing under dependency," Ann. Stat. **29**, 1165–1188 (2001).
[76]A. Landry, J. D. Spence, and A. Fenster, "Quantification of carotid plaque volume measurements using 3D ultrasound imaging," Ultrasound Med. Biol. **31**, 751–762 (2005).
[77]N. D. Nanayakkara, B. Chiu, A. Samani, J. D. Spence, J. Samarabandu, and A. Fenster, "A non-rigid image registration technique for 3D ultrasound carotid images using a 'twisting and bending' model," in *Proceedings of the 28th International Conference of the IEEE/EMBS*, New York, 30 August–3 September 2006, pp. 2738–2741.
[78]S. K. Nadkarni, D. Boughner, and A. Fenster, "Image-based cardiac gating for three-dimensional intravascular ultrasound imaging," Ultrasound Med. Biol. **31**, 53–63 (2005).